Catalysis Today 466 (2026) 115674

Contents lists available at ScienceDirect

Catalysis Today

journal homepage: www.elsevier.com/locate/cattod

Uniform sono-dispersed co-catalysts unlock superior CO_2 photoreduction on Bi_2MoO_6/TiO_2

Maryam Ahmadi [a], Seyed Mehdi Alavi [a,*], Ali Akbar Asgharinezhad [b,*], Azadeh Haghighatzadeh [c], Afsanehsadat Larimi [d,*]

[a] Catalyst and Nanomaterials Research Laboratory (CNMRL), School of Chemical, Petroleum and Gas Engineering, Iran University of Science and Technology, Tehran, Iran
[b] Chemistry and Process Research Department, Niroo Research Institute, Tehran, Iran
[c] Advanced Surface Engineering and Nanomaterials Research Center, Department of Physics, Ahv.C., Islamic Azad University, Ahvaz, Iran
[d] School of Engineering and Applied Sciences, Department of Chemical Engineering, Swansea University, Wales, UK

ARTICLE INFO

Keywords:
Bismuth molybdate
Co-catalyst
TiO_2
Photocatalyst
CO_2reduction
Sono-Dispersion

ABSTRACT

This study investigates the photocatalytic reduction of CO_2 using water vapor in a top-irradiation batch reactor, with M-Bi_2MoO_6/TiO_2 serving as the photocatalyst. Various M-Bi_2MoO_6/TiO_2 samples with different co-catalysts (M: Ni, Ce, Co, Mo, Cu) were fabricated through a deposition-ultrasound-assisted approach. The prepared samples underwent examination using UV-Vis diffuse reflectance spectroscopy (UV-Vis DRS), X-ray diffraction (XRD), Field-emission scanning electron microscopy (FESEM), N_2 adsorption-desorption isotherms, Photoluminescence (PL) and Raman spectroscopy. Methane was identified as the predominant reaction product, and the introduction of co-catalysts through sono-deposition significantly improved the photocatalytic efficiency. The catalysts with various co-catalysts showed different performances in CO_2 reduction. Additionally, the optical properties of the composite samples changed with the deposition of different co-catalysts on the BT support. Compared to pristine TiO_2, the co-catalyst-loaded composites exhibited superior CO_2 reduction performance. Among them, the Ni-BT sample had the highest methane yield, attributed to the even distribution of Ni nanoparticles, better visible-light absorption, and more effective charge separation and transfer.

1. Introduction

The escalating challenges associated with environmental pollution, resource depletion, and sustainable chemical production have motivated extensive research into advanced functional materials, where controlled composition, surface modification, and interfacial engineering play decisive roles in improving reaction efficiency and selectivity for environmental and energy-related applications [1–7]. Rising atmospheric CO_2 levels pose a severe environmental threat [8]. Photocatalytic CO_2 reduction to chemicals or hydrocarbons provides a sustainable approach to reduce global warming and fuel scarcity [9]. TiO_2 is widely studied due to its low cost, stability, and non-toxicity [10], but its wide bandgap (3.2 eV) and fast electron-hole recombination limit efficiency [11,12]. Strategies such as coupling with narrow-bandgap semiconductors [13,14], metal deposition [15,16], and doping [17–20] enhance charge separation, light absorption, and CO_2 adsorption [21–23]. Bismuth-based compounds such as Bi_2MoO_6 [24–26], Bi_2WO_6 [27], $BiVO_4$ [28], $CuBi_2O_4$ [29], and Bi-doped TiO_2 [30] are promising for environmental applications, with Bi_2MO_6 (M= W, Mo) showing bandgaps less than 3 eV suitable for visible-light activation, though rapid recombination limits their independent use [31,32]. Forming Bi_2MO_6/TiO_2 heterojunctions effectively suppresses recombination and improves photocatalytic performance [33–35].

The design of visible-light-active photocatalysts is crucial for improving the performance of TiO_2, the most prominent benchmark material in photocatalysis research, yet limited by its wide bandgap [36–40]. Co-catalysts enhance activity by facilitating charge separation at the semiconductor/co-catalyst interface and providing surface reaction sites [41]. They act as electron sinks, where electrons migrate from the semiconductor to the co-catalyst while holes remain on the catalyst, and can also improve surface adsorption for higher activity [42]. Ultrasound-assisted deposition has recently emerged as an effective method to control particle size, morphology, and dispersion of co-catalysts [43,44]. Ultrasound induces acoustic cavitation, generating

* Corresponding authors.
E-mail addresses: alavi.m@iust.ac.ir (S.M. Alavi), aashgharinezhad@nri.ac.ir (A.A. Asgharinezhad), a.larimi@swansea.ac.uk (A. Larimi).

https://doi.org/10.1016/j.cattod.2025.115674
Received 16 September 2025; Received in revised form 14 December 2025; Accepted 23 December 2025
Available online 24 December 2025

nanosized bubbles that collapse to produce high-pressure (~ 1000 bar) and high-temperature (~ 5000 K) microjets. These effects inhibit metal agglomeration, promote uniform nanoparticle formation, enhance crystallinity, and facilitate interfacial bond generation on the support surface, while also reducing catalyst preparation time [45,46].

Copper oxides have shown strong potential as co-catalysts for CO_2 photoreduction. Coupling Cu_2O/CuO with wide-bandgap semiconductors enhances light absorption and charge separation [47]. For example, Cu/TiO_2 yielded six times higher methanol than bare TiO_2, although excess Cu promoted aggregation and reduced efficiency [48]. Similarly, 10 wt% Cu on GO enhanced CO_2 conversion nearly 60-fold by suppressing recombination and narrowing the bandgap [49], while Cu/TiO_2 with 2D morphology improved methane production; excess Cu ($\geq$3 %) induced recombination centers [50]. Ni is another effective co-catalyst owing to its stability and low cost [51]. $NiO\text{-}In_3O_3/TiO_2$ showed six-fold higher activity than TiO_2 and nearly twice that of In_3O_3/TiO_2 due to efficient charge separation [14,52]. $Ni\text{-}InNbO_4$ showed superior performance to $Co\text{-}InNbO_4$, as Ni acted as an electron sink while Co promoted recombination, with 1 % $Ni\text{-}InNbO_4$ giving the best yield [53]. Other studies confirmed NiO prolongs carrier lifetime and enhances optical properties, for example, $NiO/ K_2Ta_2O_6$ produced 1815 μmol/g methanol [14,54], and $Ni\text{-}InTaO_4$ doubled methanol yield relative to $InTaO_4$ [55]. Ce and Zr also improve visible light activity [56–58]. Ce improves the CO_2 photoreduction through reversible Ce^{3+}/Ce^{4+} cycling and strong CO_2 adsorption [59]. CeO_2/CdS tripled methane yield compared to CdS [60], while 0.2 % Ce/TiO_2 increased methane production from 21 to 30 μmol/g, extending visible absorption and suppressing recombination [61]. Enhanced surface area and charge separation further improved activity by nearly three-fold over TiO_2 [62]. Mo-based co-catalysts exhibit synergistic effects; $M\text{-}WO_3$ increased methane yield almost six-fold relative to bare WO_3 [63,64]. Building on our earlier work with Bi_2WO_6/TiO_2 heterojunctions, the present study applies ultrasound-assisted deposition of transition-metal co-catalysts on Bi_2WO_6/TiO_2 to evaluate their CO_2 photoreduction performance.

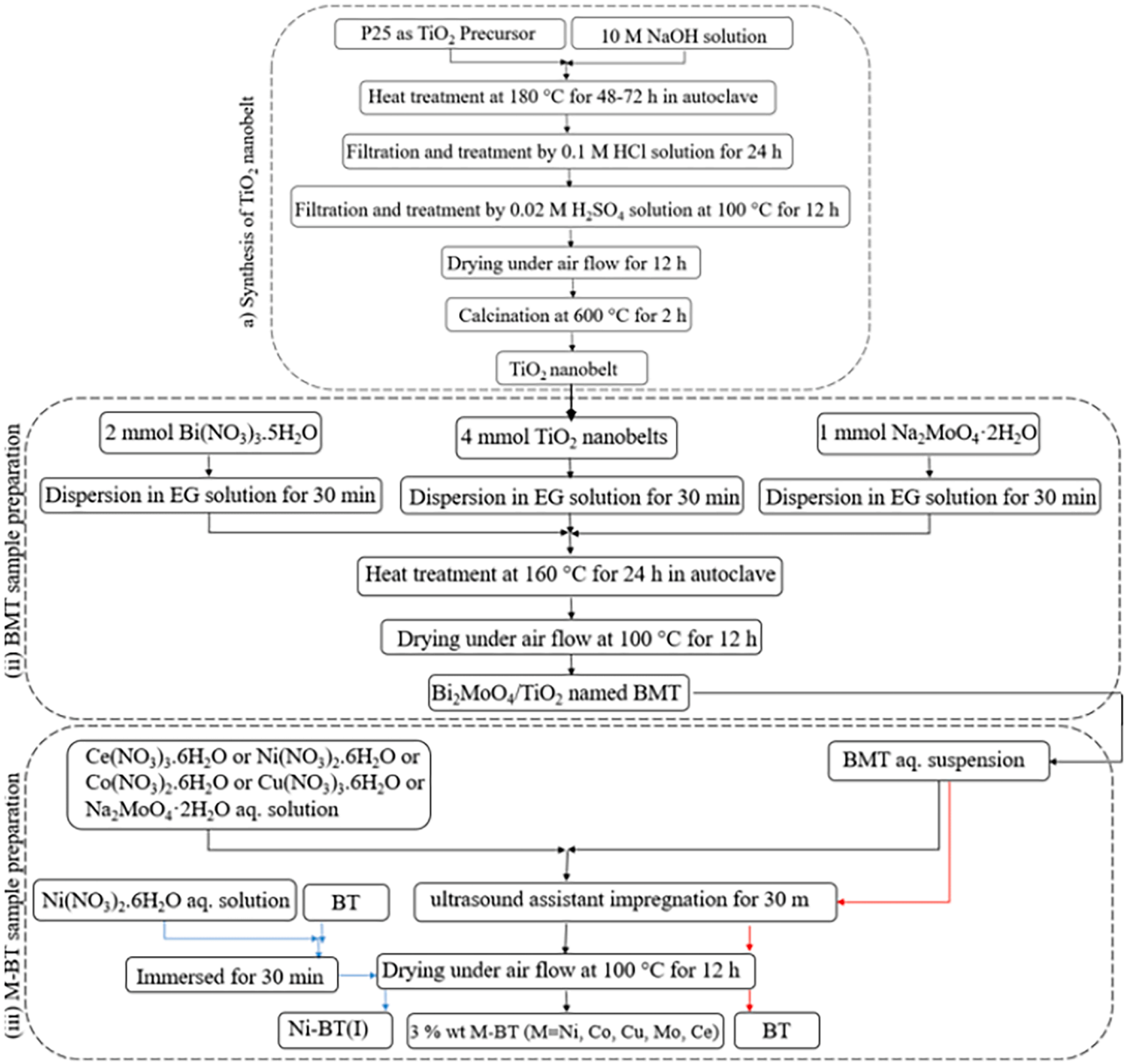

Fig. 1. Diagram of preparation steps of the TiO_2, Bi_2MoO_6, BT, Ni-BT, Co-BT, Cu-BT, Mo-BT and Ce-BT photocatalysts.

According to the literature, various co-catalysts have been utilized to enhance semiconductor efficiency in photocatalytic reactions. Transition metals are often preferred over noble metals due to their lower cost and acceptable activity. The presence of co-catalysts not only improves light absorption but also promotes reactant adsorption and charge separation. Semiconductors can act as supports, facilitating co-catalyst dispersion, while ultrasound-assisted methods ensure uniform particle distribution under mild conditions. Ultrasonic treatment induces physical and chemical modifications that optimize catalyst morphology and performance. Although ultrasound has been used for catalyst synthesis, its application in co-catalyst deposition on composite heterojunction supports has not been explored. In this study, Ni, Cu, Ce, Co, and Mo were deposited as co-catalysts on Bi_2MoO_6/TiO_2 using ultrasound irradiation to assess their impact on CO_2 photoreduction under UV-Vis light.

2. Materials and methods

2.1. Materials

Commercial P25 was utilized as the titanium source, while caustic soda (sodium hydroxide, NaOH), bismuth (III) nitrate pentahydrate [$Bi(NO_3)_3{\cdot}5H_2O$], cerium (III) nitrate hexahydrate [$Ce(NO_3)_3.6H_2O$], sodium molybdate dihydrate [$Na_2MoO_4.2H_2O$], nickel (II) nitrate hexahydrate [$Ni(NO_3)_3.6H_2O$], copper (II) nitrate hexahydrate [$Cu(NO_3)_3.6H_2O$], cobalt (II) nitrate hexahydrate [$Co(NO_3)_3.6H_2O$], hydrochloric acid (HCl), and ethylene glycol ($CH_2OH)_2$ were purchased from Merck and used without further purification. Pure water was used as the solvent for all the experiments.

2.2. Preparation of photocatalysts

Fig. 1 schematically presents the step-by-step procedure for synthesizing the M-BT photocatalysts.

2.2.1. Synthesis of TiO_2 nanobelts

Initially, 0.4 g of commercial P25 was dispersed in 80 mL of 1 M NaOH solution by vigorous stirring for 1 h. The resulting suspension was transferred into a 120 mL Teflon-lined autoclave and heated at 180 °C for 48 h. After cooling to room temperature, the precipitation was collected by filtration and repeatedly washed with pure water. The solid was then immersed in 0.1 M HCl solution for 24 h, followed by filtration and rinsing with water. Finally, the obtained material was dried at 100 °C for 12 h and calcined at 600 °C for 2 h to produce TiO_2 nanobelts.

2.2.2. Synthesis of Bi_2MoO_6/TiO_2

For the preparation of Bi_2MoO_6/TiO_2 composites, 2 mmol of $Bi(NO_3)_3{\cdot}5H_2O$, 1 mmol of $Na_2MoO_4.2H_2O$, and 4 mmol of as-prepared TiO_2 nanobelts were each dispersed in 20 mL of ethylene glycol under stirring at room temperature for 30 min to form suspensions A, B, and C, respectively. These suspensions were then combined, transferred into a Teflon-lined autoclave, and treated at 160 °C for 24 h. The resulting precipitate was collected, washed several times with pure water and dried at 100 °C for 12 h to yield the Bi_2MoO_6/TiO_2 sample (BMT).

2.2.2. Synthesis of (Ce, Ni, Cu, Mo, Co)-Bi_2MoO_6/TiO_2

To introduce co-catalysts (Ce, Ni, Cu, Mo, and Co), 3 wt% of metal precursors ($Na_2MoO_4.2H_2O$, Ce $(NO_3)_3.6H_2O$, Ni $(NO_3)_3.6H_2O$, Co $(NO_3)_3.6H_2O$ and Cu $(NO_3)_3.6H_2O$) were impregnated onto the BMT composite under ultrasonic irradiation. Ni was deposited at 1, 3, and 5 wt% onto Bi_2MoO_6/TiO_2 (BT) to screen the co-catalyst content under identical synthesis and testing conditions. The mixture of BMT support and appropriate metal salts was suspended in 30 mL of pure water and subjected to sonication using a SONOPULS HD 3200 equipped with a titanium horn (10 mm) placed 1.5 cm below the liquid surface. Sonication was applied with a pulse ratio of 1 s on/1s off at 20 kHz and 30 W for 30 min. The suspension was then dried at 100 °C for 12 h in air. The obtained catalysts were denoted as Ni-BT, Ce-BT, Mo-BT, Cu-BT, and Co-BT, corresponding to the respective co-catalysts. For comparison, a BT sample treated by ultrasound without co-catalyst loading was also synthesized under identical conditions to evaluate the role of ultrasound irradiation. Furthermore, a control sample (Ni-BT(I)) was prepared by impregnating $Ni(NO_3)_3{\cdot}6\ H_2O$ onto BT via a conventional wet impregnation method in 30 mL of pure water for 30 min, followed by drying at 100 °C for 12 h in air. This allowed assessment of the effect of ultrasound-assisted deposition on co-catalyst dispersion.

2.3. Characterization techniques

The synthesized samples were characterized by X-ray diffraction (XRD) using a PANalytical X'Pert PRO diffractometer with Cu α radiation. Diffraction patterns were recorded over a 2θ range of 10–80°. UV-Vis Diffuse Reflectance spectroscopy (UV-Vis DRS) was performed on an AvaSpec UV-Vis spectrometer, with barium sulfate as a reference, over the wavelength range of 200–1000 nm. Morphological and elemental analyses were carried out using high-resolution field-emission scanning electron microscopy (FESEM, Mira-III Tuscan) equipped with an energy dispersive X-ray (EDX) detector. N_2 absorption-desorption isotherms at 77 K were obtained using a BEL-Sorp II mini instrument, and the specific surface areas of the photocatalysts were calculated using the Brunauer-Emmett-Teller (BET) method. Raman spectra were recorded with a Tak-Ram N1–541 spectrometer using a 530 nm laser as the excitation source. Photoluminescence (PL) measurements were conducted on an Agilent G9800A spectrophotometer at an excitation wavelength of 290 nm.

2.4. Experimental configuration for catalytic performance evaluation

The photocatalytic reduction of CO_2 was conducted in a 100 mL homemade Pyrex glass reactor equipped with a quartz window at the top for illumination [65,66]. A suspension containing 100 mg of catalyst was deposited onto a glass plate and dried at 70 °C. The plate was then placed at the bottom of the reactor. All experiments were performed at ambient temperature and atmospheric pressure. Based on well-established carbonate speciation and proton-coupled electron transfer considerations, near-neutral pH was selected to ensure adequate dissolved CO_2 concentration and proton availability while suppressing competing H_2 evolution and minimizing conversion of CO_2 to bicarbonate/carbonate species. A 250 W mercury vapor lamp positioned above the quartz window served as the light source. Prior to each experiment, dry nitrogen was introduced to purge the reactor of air and other impurities. CO_2 gas was circulated through the reactor for 30 min and then passed through a water bubbler before reaching the catalyst. Water vapor was introduced by passing high-purity CO_2 (99.99 %) through a temperature-controlled bubbler containing deionized water at 25 °C. Under these conditions, the resulting gas feed contained approximately 55 % relative humidity, corresponding to a water vapor partial pressure of ~3.17 kPa. The CO_2/H_2O ratio in the reactor headspace was maintained constant during all photocatalytic experiments. Water vapor was supplied by passing high-purity CO_2 through a temperature-controlled water saturator at 25 °C, resulting in a relative humidity of ~55 % (±3 %) in the reactor headspace. The total water vapor concentration introduced was 0.021 mol H_2O per mol CO_2, corresponding to the equilibrium vapor pressure of water at 25 °C. Subsequently, the reactor inlet and outlet were closed and sealed, and the light source was turned on. After 8 h of irradiation, 1 mL of the gas sample was collected using a gas-tight syringe and analysed with a Shimadzu 2012 gas chromatograph equipped with a BP-5 column and a flame ionization detector (FID). Before each experiment, the reactor was purged with dry nitrogen for 30 min to remove any residual species weakly absorbed on the catalyst surface. Methane was identified as the primary hydrocarbon product, while other hydrocarbons were detected only in trace amounts. The methane yield was reported in μmol/g of catalyst. Blank

experiments were conducted in the absence of catalyst, light, or CO_2 to confirm that methane formation required the presence of all three components. The reactor temperature was maintained using two fans installed in the system box. All experiments were conducted in triplicate under identical conditions, with an experimental error of less than 3 %. The CO_2 photocatalytic reduction performance can also be measured by apparat quantum yield (AQY) (%), which can calculate using number of reacted electrons to generate each product and number of incident photons

3. Results and discussions

3.1. Characterizations

3.1.1. XRD

The XRD patterns of double and triple as-prepared composites are presented in Fig. 2. Pure TiO_2 nanobelts exhibited the characteristic anatase phase (JCPDS, No. 21–1272) with diffraction peaks at 2Θ= 25.3 ° and 47.6 ° [67,68]. The BMT double composite showed diffraction peaks at 2Θ= 28.4 °, 32.7 °, 46.6 ° and 55.6 °, corresponding to the orthorhombic structure of Bi_2MoO_6 (JCPDS No.72- 1524) [69,70], along with a weak peak at 2Θ= 47.6° attributed to TiO_2 anatase phase. The presence of characteristic peaks of both Bi_2MoO_6 and TiO_2 in the BMT sample indicates the successful fabrication of BMT heterostructure and strong interaction between Bi_2MoO_6 and TiO_2. The positions of the characteristic peak remained unchanged, confirming that Bi_2MoO_6 is not incorporated into the TiO_2 lattice and both phases remain separate [71]. The intensity of the characteristic peaks slightly decreased after ultrasound modification, consistent with previous reports [72,73]. All ultrasound-modified BT samples displayed peaks corresponding to both TiO_2 and Bi_2MoO_6. No diffraction peaks related to Mo oxide were observed in the Mo-BT sample, suggesting low loading or high dispersion of Mo on the support [74]. Similarly, Co-BT showed no detectable Co peaks, indicating very small particle size [53]. The absence of peaks related to nickel oxide in the Ni-BT sample may be due to the low amount of Ni below the XRD detection limit or the high distribution of Ni on the BT support [14]. The XRD pattern of Cu-BT was similar to that of BT, and no signals corresponding to Cu species were detected, which may be attributed to low co-catalyst loading or high particle dispersion [48]. Although co-catalyst peaks were not detected by XRD, their presence on the BT support was confirmed by EDX dot-mapping images. The crystalline structure of BT remained intact after ultrasound treatment, and all modified photocatalysts exhibited similar peak positions. No characteristic peaks corresponding to CeO_2 or other co-catalysts were observed, indicating that the co-catalysts were well-dispersed on the BT composite, consistent with EDX results. Ultrasonic irradiation generates localized hot spots that facilitate interactions between co-catalysts and the composite, promoting nucleation, dispersion, and the formation of nanometric metal particles [75]. Consequently, ultrasound-assisted deposition enhances co-catalyst dispersion on the BT support, improving accessibility for reactant molecules and potentially increasing photocatalytic performance. This observation is further supported by CO_2-TPD analysis. Therefore, it is expected that ultrasound-assisted synthesized co-catalyst-containing samples exhibit satisfactory photocatalytic activity for CO_2 reduction.

3.1.2. DRS

The UV–vis DRS spectra of BT photocatalysts containing different co-catalysts are presented in Fig. 3, within the range of 350–800 nm. Pure TiO_2 exhibited an absorption edge in the ultraviolet region, consistent with its wide bandgap, whereas BT displayed a red-shifted absorption edge extending into the visible region due to its narrow bandgap. The optical bandgap values were calculated from DRS data using the Tauc plot of the Kubelka-Munk function. The optical bandgap values were estimated using diffuse reflectance spectroscopy (DRS) combined with the Kubelka–Munk transformation and Tauc plot analysis, which is a widely accepted approach for semiconductor powders. The Kubelka–Munk function converts reflectance data into a quantity proportional

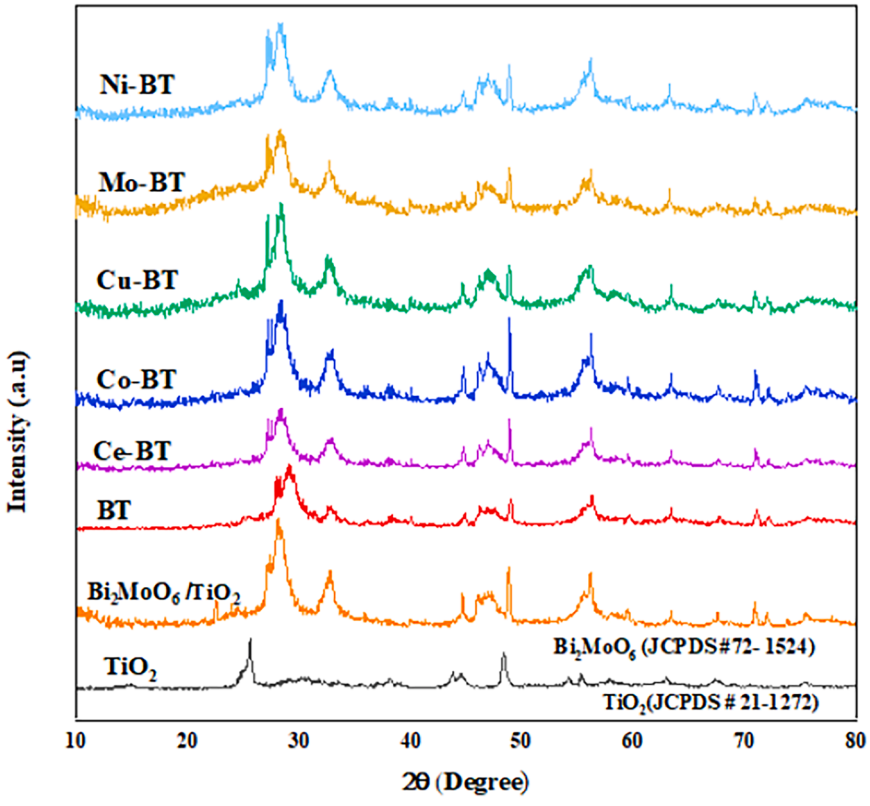

Fig. 2. XRD patterns of TiO_2, Bi_2MoO_6/TiO_2, BT, Ni-BT, Co-BT, Cu-BT, Mo-BT and Ce-BT samples.

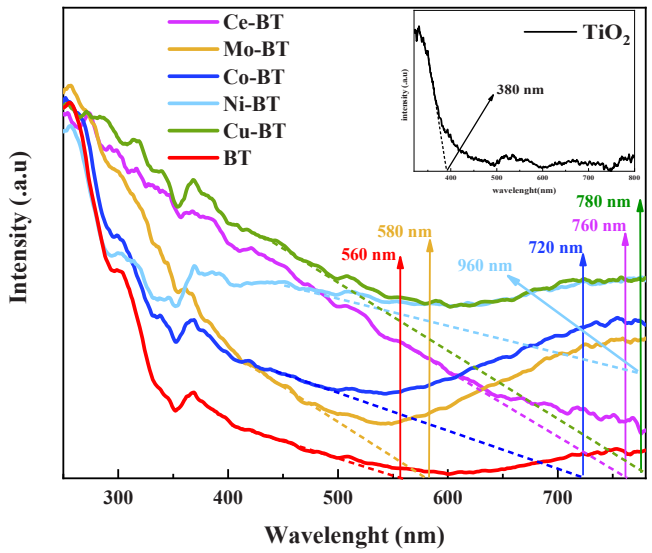

Fig. 3. UV–Vis absorption spectra of TiO_2, BT, Ni-BT, Co-BT, Cu-BT, Mo-BT and Ce-BT samples.

to the absorption coefficient, enabling reliable bandgap estimation in highly scattering materials. Previous studies have demonstrated that bandgap values obtained from DRS–Tauc analysis are in good agreement with those derived from conventional UV–Vis absorption measurements, particularly for TiO_2-based and doped oxide photocatalysts, confirming the validity of this method for comparative optical analysis [76,77]. As summarized in Table 1, the bandgap was 3.2 eV for TiO_2, 2.4 eV for BT, and 2.02, 2.03, 2.08, 2.09, and 2.1 eV for Ni-BT, Cu-BT, Ce-BT, Co-BT, and Mo-BT, respectively. Compared with BT, all co-catalyst-modified composites exhibited enhanced absorption in the visible region, which is attributed to the deposition of co-catalysts on the BT support. The broader absorption of these samples allows for the utilization of a larger portion of the solar spectrum, thereby improving photocatalytic efficiency [47,53]. Specifically, Ce loading extended light absorption, consistent with previous findings [61]. The Co-BT sample demonstrated pronounced absorption across the UV–Vis region, while pure TiO_2 showed negligible absorption beyond 385 nm [78]. The Mo-BT sample displayed a spectral shape similar to BT but with higher overall intensities, suggesting the incorporation of Mo particles on the BT surface [74]. Similarly, Cu deposition extended optical absorption, which agrees with earlier reports [79]. Among the modified samples, Ni-BT exhibited the narrowest bandgap. This red-shift can be attributed to improved charge migration and the possible formation of Ni/Ti-O bands, which reduce the excitation energy of photogenerated carriers [80]. The absorption edge shift is a direct indicator of changes in the electronic band structure, which can influence the photocatalytic properties. A red-shift in the absorption edge was observed for the Ni-modified sample, indicating a narrowing of the bandgap. This is likely due to the synergy between Ni and the semiconductor components (Bi_2MoO_6 and TiO_2), which enhances light absorption, particularly in the visible region. Moreover, the localized surface plasmon resonance (LSPR) of dispersed Ni particles further lowered the bandgap energy. Acting as electron sinks, Ni nanoparticles provided sites for electron accumulation and migration, thereby suppressing the recombination of electron-hole pairs and enhancing charge separation efficiency [37].

Table 1
Physiochemical properties of photo-catalysts.

Photocatalyst	BET surface area (m^2/g)	Pore volume (cm^3/g)	Average pore diameter (nm)	Band gap (eV)	CH_4 yield (μmol. g^{-1}. h^{-1})	AQY (%)
TiO_2	22	0.072	13.24	3.2	3.2	0.084
BMT	28	0.091	11.01	2.8	36.1	0.948
BT	33	0.123	9.8	2.4	39	1.025
Ni-BT	31	0.105	11.04	2.02	53.7	1.411
Cu-BT	30	0.103	11.93	2.03	49.6	1.304
Ce-BT	29	0.099	12.04	2.08	47.1	1.238
Co-BT	28	0.086	12.9	2.09	41.5	10.90
Mo-BT	26	0.078	12.94	2.1	38.4	1.009

3.1.3. FESEM and EDX

The surface morphologies of the as-synthesized samples were examined using FESEM analysis. Pure TiO_2 exhibited a nanobelt structure (Fig. 4a). In the BMT composite, Bi_2MoO_6 nanosheets were clearly observed on the TiO_2 nanobelts (Fig. 4b). The BT sample showed a nanoplate-like structure (Fig. 4c), and distinct morphological changes were evident after ultrasound modification. Furthermore, the TEM image of the Ni-BT (Fig. 4i) confirmed the presence of uniform plate-shaped particles. A large number of homogeneous nanoparticles were consistently observed across all co-catalyst-modified samples. The surface morphology of the Ni–BT sample was examined using SEM, as shown in Fig. 4g. The images reveal that Ni nanoparticles are uniformly distributed on the BT surface, forming nearly spherical aggregates. A statistical analysis of the Ni particle size distribution was carried out using ImageJ software based on measurements of more than 100 particles. The results indicate that the Ni nanoparticles possess an average diameter of approximately 25 ± 5 nm, with particle sizes ranging from 15 to 35 nm, confirming a relatively narrow size distribution. Such homogeneous dispersion of Ni nanoparticles is expected to enhance the surface area and improve the catalytic/electronic properties of the Ni–BT composite.

The EDX elemental mapping further confirmed the uniform distribution of Ti, O, Bi and Mo in the BT sample (Fig. 5). Co-catalyst elements were also uniformly dispersed on the BT support, which is consistent with the XRD and FESEM observations. Such homogeneous dispersion ensures intimate contact between co-catalyst and support, thereby promoting the generation and migration of photoinduced charge carriers [81]. Ultrasound irradiation was found to play a crucial role in controlling particle size and morphology. The acoustic cavitation effect promoted smaller particle formation, improved particle distribution, and enhanced co-catalyst dispersion on the BT surface [44,73,82]. Consequently, the synthesized nanometric catalysts provided more accessible active sites, contributing to higher photocatalytic activity. Overall, FESEM and EDX analyses revealed that while the general morphologies of the modified samples remained comparable, ultrasound-assisted deposition resulted in more uniform co-catalyst dispersion and improved surface properties, which are favourable for photocatalytic performance.

3.1.4. N_2 Physisorption

The specific surface area is a crucial factor that influences light absorption, reactant adsorption, and ultimately the photocatalytic performance. The nitrogen adsorption-desorption isotherms of BT and co-catalyst-modified samples (Ni-BT, Cu-BT, Ce-BT, Co-BT, and Mo-BT) are shown in Fig. 6a, while the corresponding BJH pore size distributions are presented in Fig. 6b. All samples exhibited type IV isotherms with an H3 hysteresis loop, according to the IUPAC classification [83–85]. The appearance of hysteresis at high relative pressure suggests the presence of mesopores formed by the aggregation of sheet-like particles, leading to slit-shaped pores [71]. These observations are consistent with the FESEM results. The pore size distributions indicate an average pore diameter in the range of 13–22 nm, confirming the mesoporous nature of the samples. Such a structure is beneficial for photocatalytic reactions, as smaller pore sizes reduce mass-transfer limitations and enhance surface-based processes [14]. The BET surface area of the as-prepared samples is summarized in Table 1. Pure TiO_2 exhibited a surface area of 21.8 m^2/g, which increased to 24.9 m^2/g upon Bi_2MO_6 incorporation in the BT composite. However, the

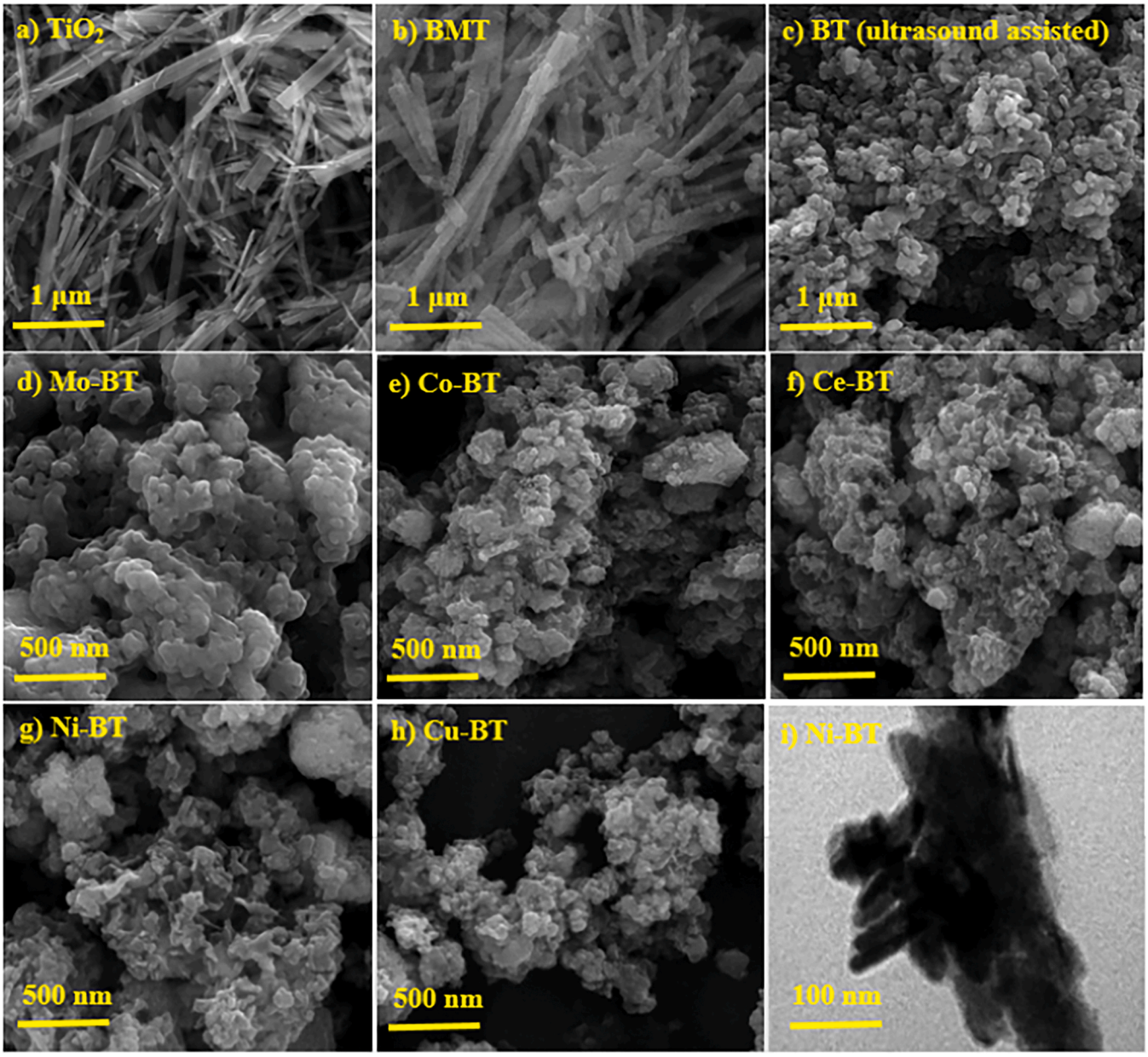

Fig. 4. (a-h) FESEM images for BT, Ni-BT, Co-BT, Cu-BT, Mo-BT, and Ce-BT samples, and (i) TEM image for Ni-BT sample.

deposition of co-catalysts by ultrasound generally led to a decrease in surface area (from 21.4 to 12.7 m^2/g), indicating that co-catalyst loading partially blocked the surface pores. Although the BET specific surface area decreases upon loading the Ni co-catalyst, the catalytic activity increases markedly. This apparent paradox can be reconciled by interfacial phenomena rather than geometric area alone. First, electronic metal–support interactions modify the local electronic structure at the Ni–support perimeter, enhance interfacial charge transfer, and stabilize active configurations, collectively boosting turnover despite partial pore coverage [86]. Second, the co-catalyst furnishes intrinsically active reduction/oxidation sites that lower activation barriers for the surface half-reactions and improve utilization of electrons/holes at the interface [87]. Third, in heterojunctions the built-in interfacial electric field drives directional carrier migration (e^- to the reduction side; h^+ to the oxidation side), suppressing recombination and amplifying reaction rates even when the total surface area is lower; our PL quenching trends are consistent with this mechanism [88]. Among the co-catalyst-modified composites, Ni-BT retained the highest surface area. This relatively large surface area can promote higher reactant adsorption, thereby contributing to enhanced CO_2 photoreduction efficiency.

3.1.5. *Photoluminescence (PL) Spectroscopy*

Fig. 7 displays the PL spectra of TiO_2, BT, and co-catalyst-modified BT (M-BT) samples. Pure TiO_2 showed a strong emission peak at around 580 nm, attributed to the recombination of photogenerated charge carriers. The incorporation of Bi_2MoO_6 resulted in a decrease PL intensity of BT compared to TiO_2, indicating a lower recombination probability and more efficient separation of photoinduced electron-hole pairs. All samples excited at 290 nm exhibited a broad emission band between 550 and 600 nm, with a peak maximum centered around 580 nm. The reduced PL intensity of BT relative to TiO_2 was due to the formation of a Bi_2MoO_2/TiO_2 heterojunction, which promoted separation and suppressed recombination. Additionally, the deposition of metallic co-catalysts on BT (triple composites) further decreased PL intensity. This reduction was attributed to the uniform dispersion of co-

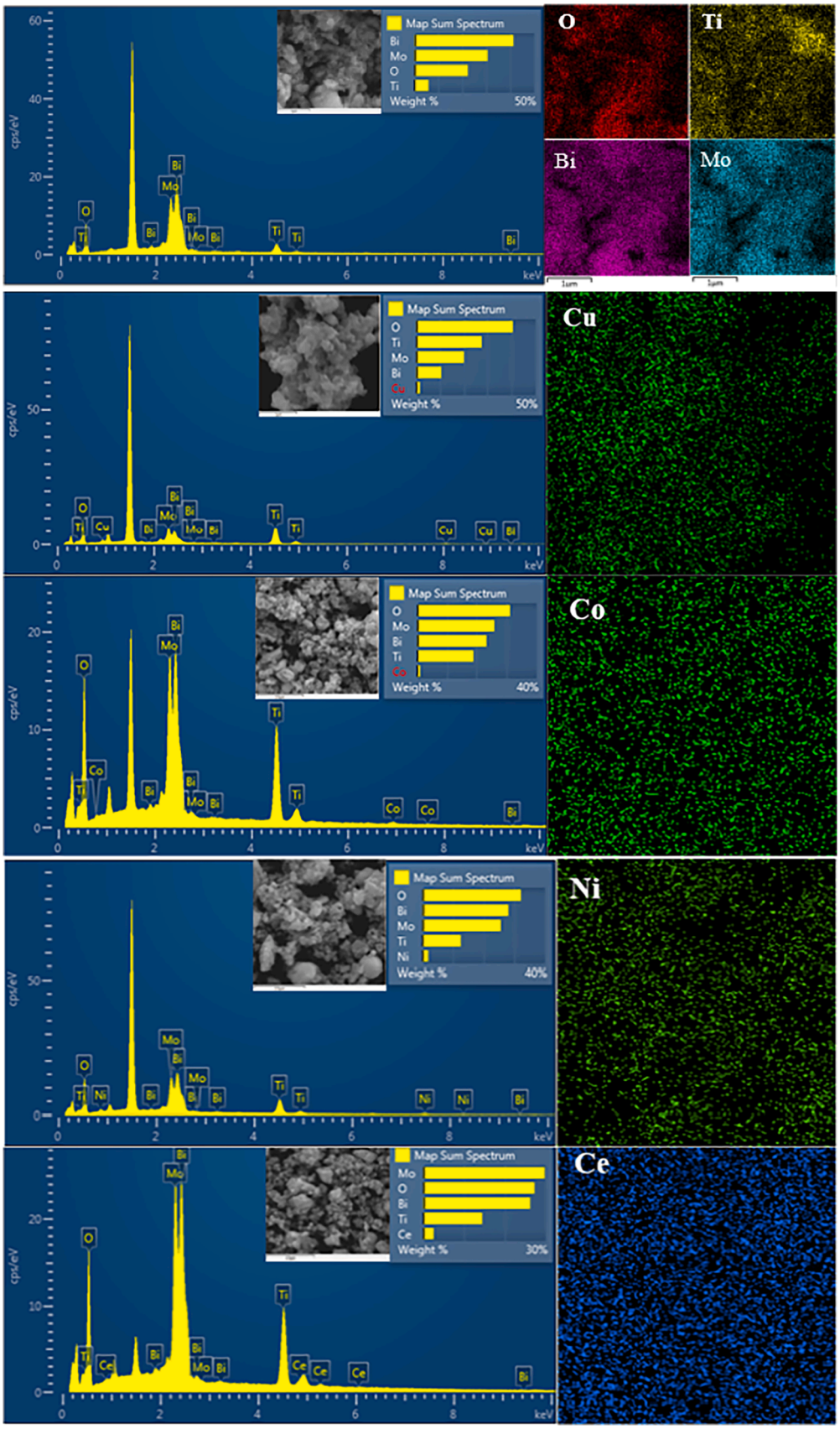

Fig. 5. EDX analysis of BT, Ni-BT, Co-BT, Cu-BT, Mo-BT and Ce-BT samples.

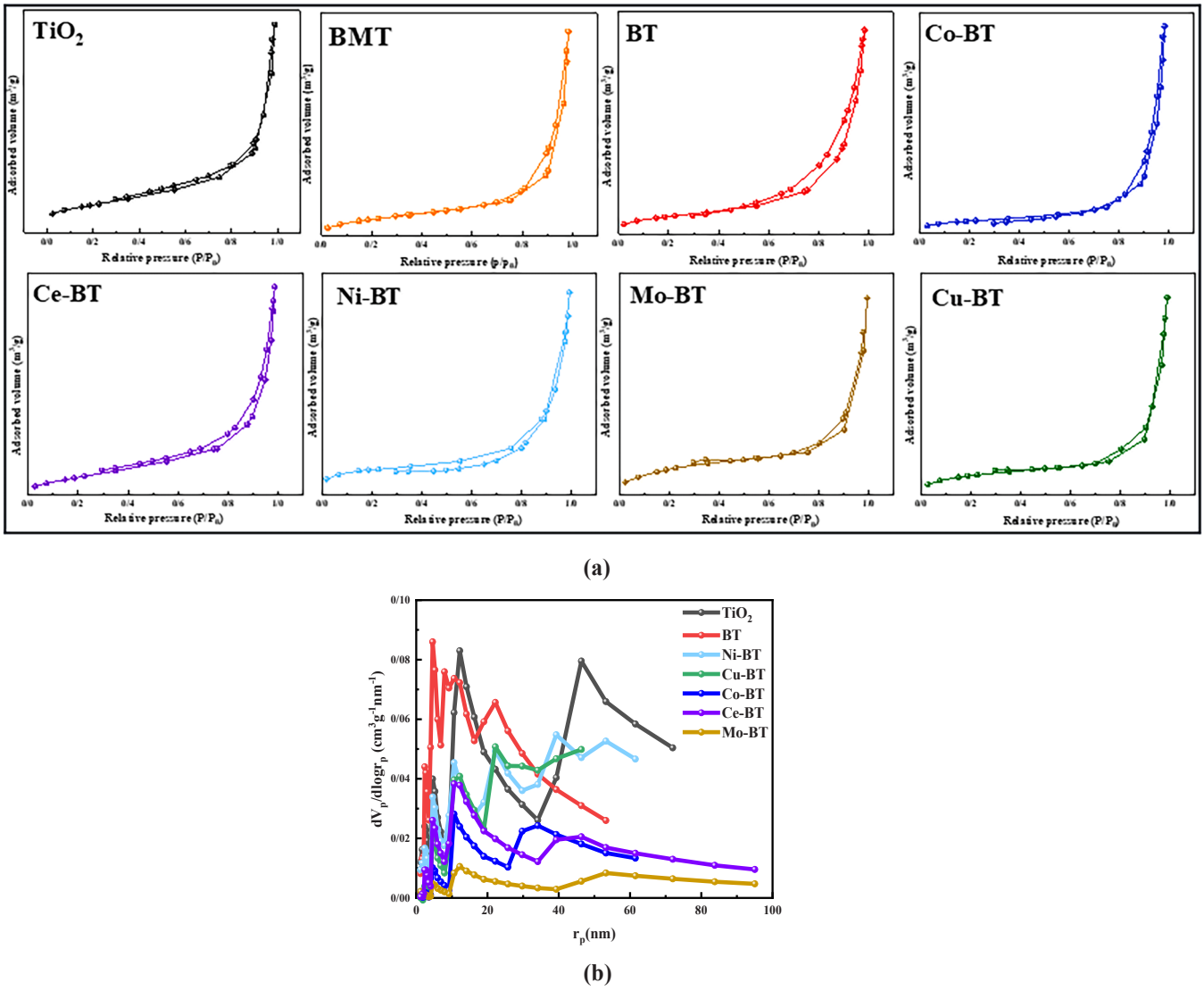

Fig. 6. a N2 adsorption–desorption isotherms for catalyst samples. b Pore size distribution of samples.

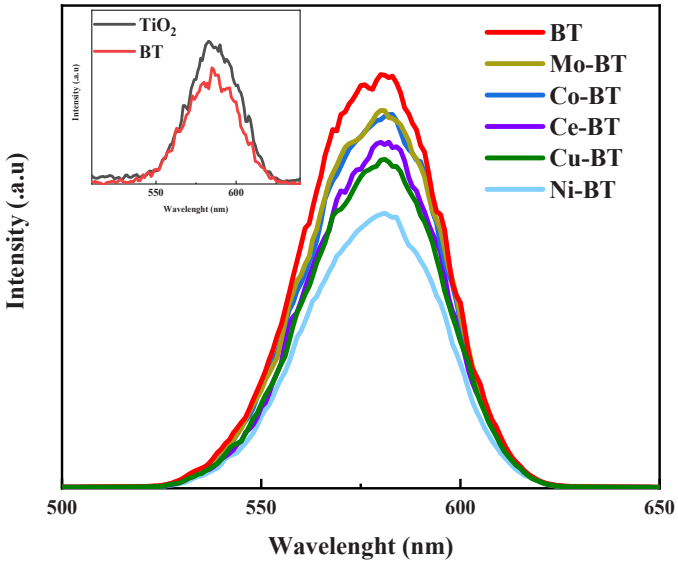

Fig. 7. Photoluminescence spectra of synthesized photocatalysts.

catalyst particles, achieved through ultrasound irradiation, enhancing interfacial interactions and providing efficient trapping sites for photogenerated charges. The significant quenching of PL signals in M-BT composites indicated that the co-catalyst loading effectively suppressed electron-hole recombination, thereby improving charge separation efficiency. The results of the PL analysis in this study provide strong evidence that Ni acts as an electron sink, facilitating charge separation and enhancing photocatalytic performance. This behaviour directly correlated with the enhanced photocatalytic activity of these composites for CO_2 reduction, particularly in methane generation [89,90].

The electrochemical impedance spectroscopy (EIS) of as-prepared samples were applied to provide more insight into the transfer of photoexcited charge carriers (Fig. 8). It should be noted that the arc radius size in the EIS plot exhibits the resistance of charge migration at the interface of semiconductor-electrolyte. Thus, the smaller radius exhibits lower charge transfer resistance, higher photoexcited charge transport and higher carrier separation efficiency. Among all the samples, the Ni–BT composite shows the smallest semicircle radius, suggesting the lowest arc radius value and, consequently, the most efficient separation and transport of photogenerated charge carriers. In contrast, bare TiO_2 and Bi_2MoO_6 display much larger arcs, implying sluggish charge transfer and severe recombination. The moderate semicircle sizes of Ce–BT, Co–BT, Mo–BT, and Cu–BT indicate partial improvements that

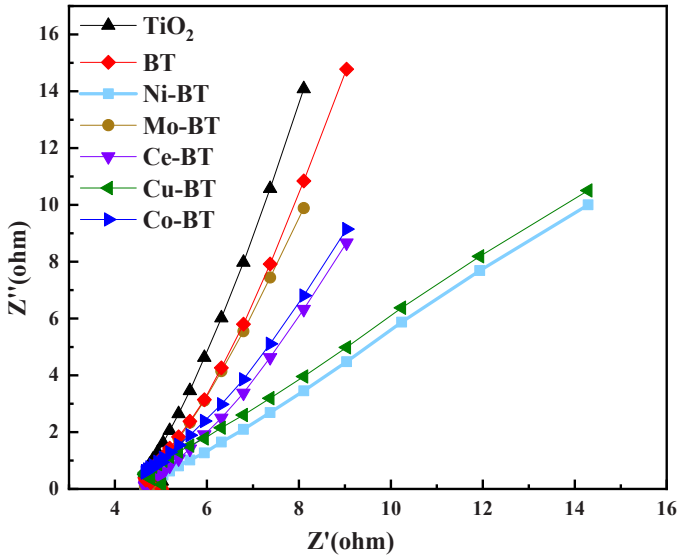

Fig. 8. Electrochemical impedance spectroscopy (EIS) of synthesized photocatalysts.

depend on the intrinsic redox properties and dispersion uniformity of each cocatalyst. These results confirm that ultrasonic-assisted Ni deposition greatly enhances the interfacial electron mobility between Bi_2MoO_6 and TiO_2, promoting efficient charge migration to the Ni active sites, where adsorbed CO_2 molecules undergo multielectron reduction to CH_4. The improved conductivity and suppressed recombination observed here are consistent with the lower PL intensity of Ni–BT. Thus, Ni nanoparticles act as electron mediators to accelerate interfacial transport and strengthen CO_2 reduction efficiency.

3.1.6. *Raman analysis*

Fig. 9 shows the Raman spectra of the as-prepared photocatalysts. The TiO_2 nanobelts exhibited bands at 145 ($E_{1\,g}$), 398 ($B_{1\,g}$), 518 ($A_{1\,g}$), and 640 ($E_{2\,g}$) cm^{-1}, corresponding to the TiO_2 anatase phase [14]. The peaks at 145 and 640 cm^{-1} were associated with O–Ti–O symmetric stretching vibrations, while the peaks at 398 and 518 cm^{-1} were related to the counter-bending and symmetric bending vibrations of O–Ti–O [91]. In the BT sample, the bands at 590 ($A_{1\,g}$) and 890 ($A_{2\,u}$) cm^{-1} were assigned to characteristic peaks of Bi_2MoO_6 [92]. These bands corresponded to the symmetric and asymmetric bending vibrations of the MoO_6 octahedra, respectively. [93]. The results demonstrated that loading Bi_2MoO_6 on the TiO_2 surface decreased the intensity of Raman characteristic peaks of TiO_2, consistent with the XRD patterns. A significant shift in the Ti–O or Mo–O vibration modes in the composite suggests that the interaction between the Ni species and the semiconductor phases could enhance charge carrier dynamics and photocatalytic activity. No peaks corresponding to Ni, Cu, Ce, Co, or Mo co-catalysts were observed in the modified BT photocatalysts, which may have been due to the low metal loading and/or the high dispersion of metal species on the BT support [94]. Moreover, no additional peaks were detected in the Raman spectra of the triple composite samples, which was consistent with the XRD results.

3.2. *CO_2 photo-reduction activity*

Fig. 10 displays the CO_2 photocatalytic conversion over the as-prepared photocatalysts under UV–visible light irradiation for 8 h in the presence of water vapor. Methane was identified as the main product in the gas phase. No methane was detected in the control experiments, which indicated that the generation of products resulted from the co-existence of photocatalyst, CO_2 and light irradiation. The ^{13}C isotope labeling test was carried out in similar reaction condition to confirm the

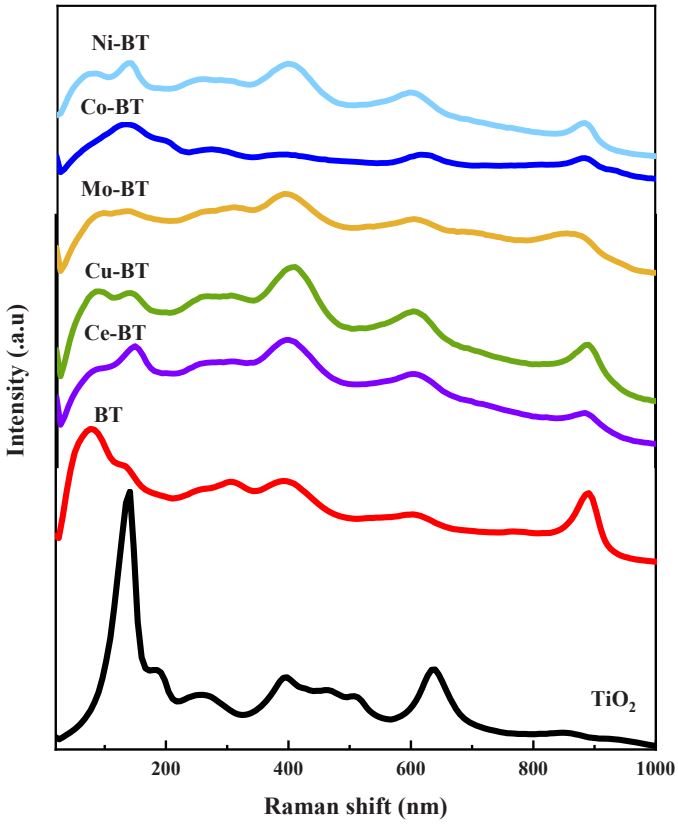

Fig. 9. Raman spectra of samples.

CO_2 reduction (Fig. 11). The CO_2 isotope test confirmed that methane product was generated from CO_2 reactant [95]. CO_2 was the main carbon source to produce methane using Ni-BT sample. Signal at $m/z = 17$ related to $^{13}CH_4$ detected by GC-MS (Agilent MS-5973 GC-mass spectroscopy) when $^{13}CO_2$ was utilized as reactant and methane was generated which demonstrated that methane generated from CO_2 photoreduction. To investigate the influence of co-catalysts on methane production, a series of catalysts were prepared using different metals at constant quantities and support. The modified photocatalysts with deposited metal oxides as co-catalyst exhibited higher photocatalytic activity than the BMT sample. Ultrasound modification led to homogenous dispersion of metal particles on the BMT support, reduced particle agglomeration, and suggested a strong interaction between metal particles and the BMT support, which resulted in a lower recombination rate of photoexcited electron-holes and enhanced reactant molecule absorption, thereby improving photocatalytic performance. The addition of co-catalyst further decreased the recombination rate of photogenerated electron-holes by serving as electron sinks, while holes remained on the support. As expected, the triple composites showed higher methane production than the BT sample. This enhancement was attributed to improved structural and optical properties, including fine dispersion of metal particles, uniform morphology, and strong interaction between metal particles and support, as confirmed by XRD, FESEM, EDX and PL analysis. To identify the optimum co-catalyst content, we prepared a series of Ni-loaded Bi_2MoO_6/TiO_2 (denoted xNi-BT, x = 1, 3, 5 wt%). As summarized in Table 2, increasing Ni from 1 to 3 wt% enhanced the methane production rate from 47.0 μmol g^{-1} to 53.7 μmol g^{-1} under otherwise identical conditions, while a further increase to 5 wt % led to a lower activity (48.2 μmol g^{-1}). This volcano-type behavior is consistent with the general understanding that moderate co-catalyst loadings promote charge separation and furnish additional surface redox sites, whereas excessive metal coverage can partially shade the light-harvesting surface and introduce additional recombination centers

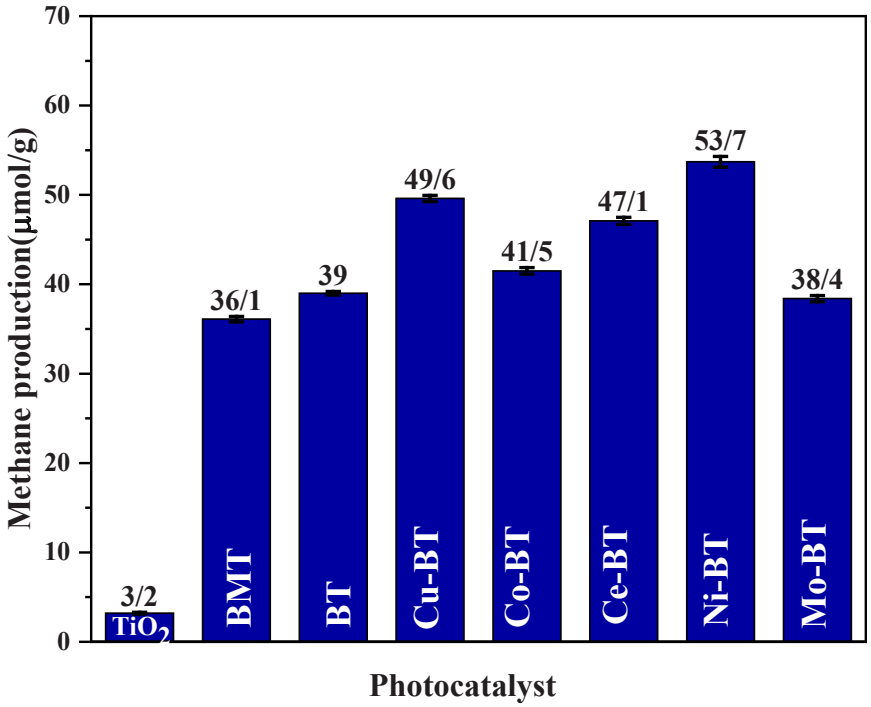

Fig. 10. CH_4 yield over different photo-catalysts after 8 h of reaction.

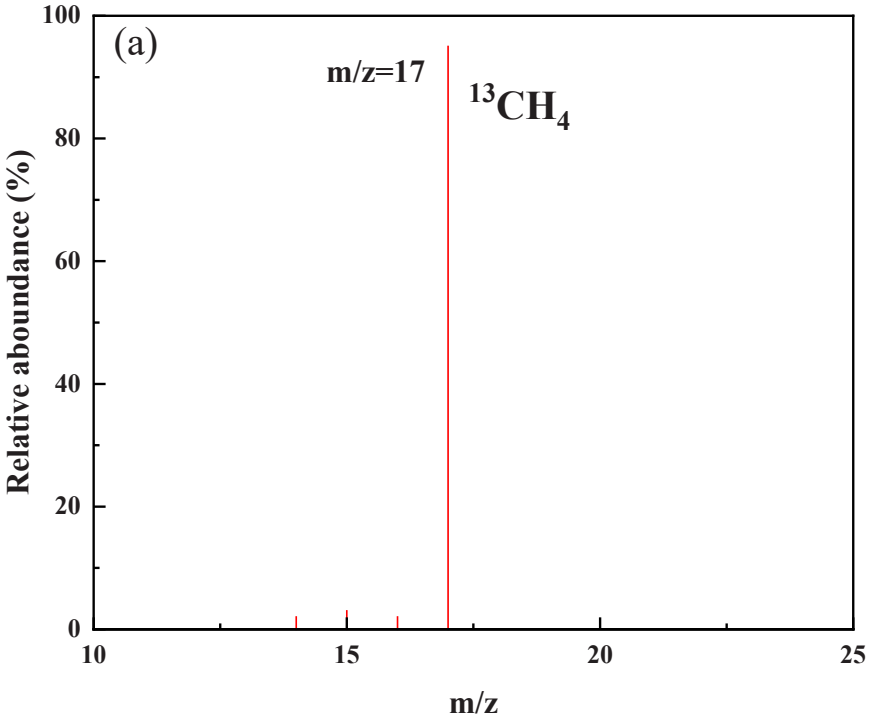

Fig. 11. ^{13}C isotope labeling test on Ni-BT sample.

Table 2
CH_4 productivity as a function of Ni loading on Bi_2MoO_6/TiO_2

Photocatalyst	Ni loading (wt%)	CH_4 yield (μmol.g^{-1}.h^{-1})
1Ni-BT	1	47.0
3Ni-BT	3	53.7
5Ni-BT	5	48.2

[96]. In line with prior observations on TiO_2-based systems where the "rise–plateau–decline" trend appears upon increasing metal loading, we therefore identify 3 wt% Ni as the optimal content for the Bi_2MoO_6/TiO_2 platform in this work [97]. Methane production after 8 h of irradiation was measured as 26.1 μmol/g for the BT sample, whereas Cu-BT, Co-BT, Ce-BT, Ni-BT, and Mo-BT samples produced 39.6, 41.5, 47.1, 53.7, and 38.4 μmol/g, respectively. The Ni-BT sample demonstrated the highest methane production, surpassing TiO_2, the reference sample, by

approximately 13 times. Additionally, the BT sample exhibited superior photocatalytic performance compared to the BMT sample, suggesting that ultrasound modification increased the surface area and provided an appropriate morphology, as confirmed by BET and FESEM results. The maximum apparent quantum yield (AQY) of methane production was achieved 1.411 % on Ni-BT sample, which is about 5 times higher than pure TiO_2 sample (Table 1).

The rate of CO2 photocatalytic reduction varied with the loading of Ce on BT. The ceria co-catalyst enhanced charge separation efficiency, contributing to the improved catalytic activity of the Ce-BT sample [60]. Introduction of cobalt as a co-catalyst improved the photo-response of the BMT support. Furthermore, due to the electron sink effects of Co and the generation of an internal electric field, the separation of the photoexcited charge carriers was increased, resulting in superior photocatalytic performance of Co-BT compared to BT [98]. The presence of Mo in Mo-BT provided a shorter distance for photoinduced electron-hole migration and reduced charge carrier recombination, leading to higher effectiveness than BT [74]. The formation of an electric field at the Cu-BT interface enriched the electron density on the catalyst surface, thereby enhancing the photocatalytic performance of Cu-BT [79]. The superior photocatalytic performance of Ni-BT was attributed to its high visible light absorption capacity, narrow bandgap, uniform particle distribution, strong interaction between nickel oxide and BT support and high separation efficiency of photoinduced electron-hole pairs, as verified by DRS, XRD, FESEM, EDX, and PL analyses.

The stability test of the Ni-BT sample for CO2 photocatalytic reduction is shown in Fig. 12. Methane production over Ni-BT was evaluated for four consecutive cycles under conditions identical to the experimental setup. The photocatalytic activity was maintained without a noticeable decrease in CO_2 conversion during the four runs, suggesting the sufficient stability of the Ni-BT sample for methane generation. where sustained photocatalytic activity after several cycles is used as evidence of both performance and structural stability (e.g., cyclic tests showing negligible activity loss over multiple runs). In addition, morphology and elemental composition remain largely unchanged after cyclic photocatalytic experiments, further supporting durability evaluations based on performance tests. The photocatalytic conversion of CO_2 into methane involved multiple steps. The initial step was the adsorption and activation of CO_2, which depended on the catalyst surface properties. FESEM and BET analyses confirmed the potential of CO_2 adsorption on the catalyst surface. The photocatalytic reduction of CO_2 was a complex multi-electron process that involves the generation of photoexcited charge carriers, their migration, the cleavage of C-O-C bonds, and the subsequent formation of C-H bonds. The presence of nickel oxide was verified by EDX analysis.

Since the photocatalytic reaction is strongly influenced by the band structure and redox potential of the catalyst, the proposed mechanism for the Ni-BT sample is illustrated in Fig. 13. The valence band (E_{VB}) and conduction band (E_{CB}) potentials of Bi_2MoO_6 and TiO_2 were calculated using the equations $E_{VB} = X\text{-}E^e + 0.5E_g$ and $E_{CB} = E_{VB}\text{-}E_g$, where X represents the absolute electronegativity of the semiconductor (5.55 for Bi_2MoO_6 and 5.81 for TiO_2), E^e is the free electron energy of hydrogen (4.5 eV), and E_g denotes the bandgap energy (2.8 eV for Bi_2MoO_6 and 3.25 eV for TiO_2) [99] Based on calculations, the E_{CB} and E_{VB} values of Bi_2MoO_6 were estimated to be −0.35 and 2.45 eV, respectively, while those of TiO_2 were −0.29 and 2.91 eV. The alignment of band edges suggests that Bi_2MoO_6 and TiO_2 can form a type (II) heterojunction, which facilitates charge separation. Under illumination, photoinduced holes migrate from TiO_2 to Bi_2MoO_6, while electrons transfer from Bi_2MoO_6 to TiO_2, effectively suppressing recombination. For selective CO_2 reduction, the conduction band of the catalyst must be at a potential more negative than the redox potential of the target product. The reduction potentials of CO_2 to CO and CH_4 are −0.53 eV and −0.24 eV, respectively. Since the conduction band of TiO_2 (-0.29 eV) is more negative than the reduction potential of CO_2/CH_4 (-0.24 V), electrons in the TiO_2 conduction band can participate in the reduction of adsorbed CO_2 to methane. Similarly, the valence band of Bi_2MoO_6 (2.45 eV) is more positive than the oxidation potential of H_2O/H^+ (0.82 eV), indicating that photogenerated holes in the Bi_2MoO_6 can oxidize water to produce protons. As a result, electrons and protons combine to form CH_4, which requires the transfer of eight photoinduced electrons [100]. Upon light irradiation, electrons in the valence band of the semiconductors are excited to the conduction band, leaving behind holes. While some electron-hole pairs recombine, others participate in redox reactions. Nickel loading is proposed to further enhances this process by serving as an electron trap, since the reduction potential of Ni (-0.24 eV) is slightly more positive than that of the TiO_2 conduction band (-0.29 eV). This is expected to promote electron accumulation on Ni sites, prolong charge carrier lifetimes, and enhance methane formation. Additionally, the potential formation of a p-n junction between BT and NiO is proposed to create an internal electric field that further facilitates charge separation, allowing electrons to migrate efficiently toward NiO while holes move in the opposite direction [80,101–103].

Literature reports indicate that the conduction band edge of nickel oxide (Ni^{2+}/Ni) lies at a sufficiently negative potential (-0.24 eV) to thermodynamically enable CO_2 reduction into methane [14]. However,

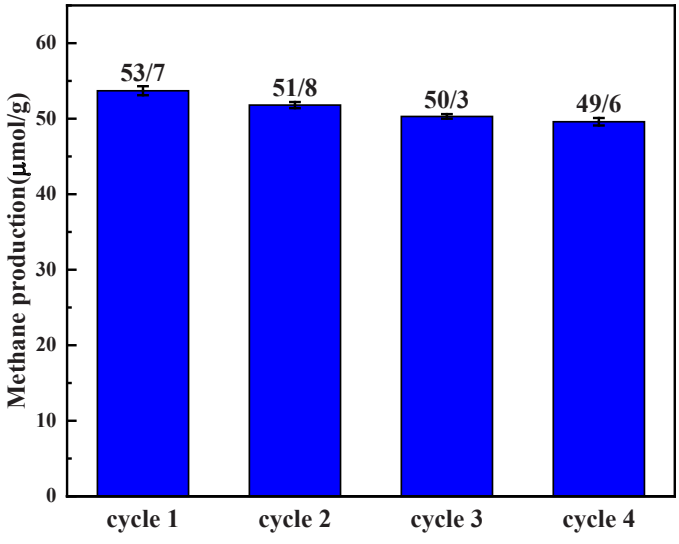

Fig. 12. CH_4 yield of Ni-BT sample during consecutive photocatalytic tests.

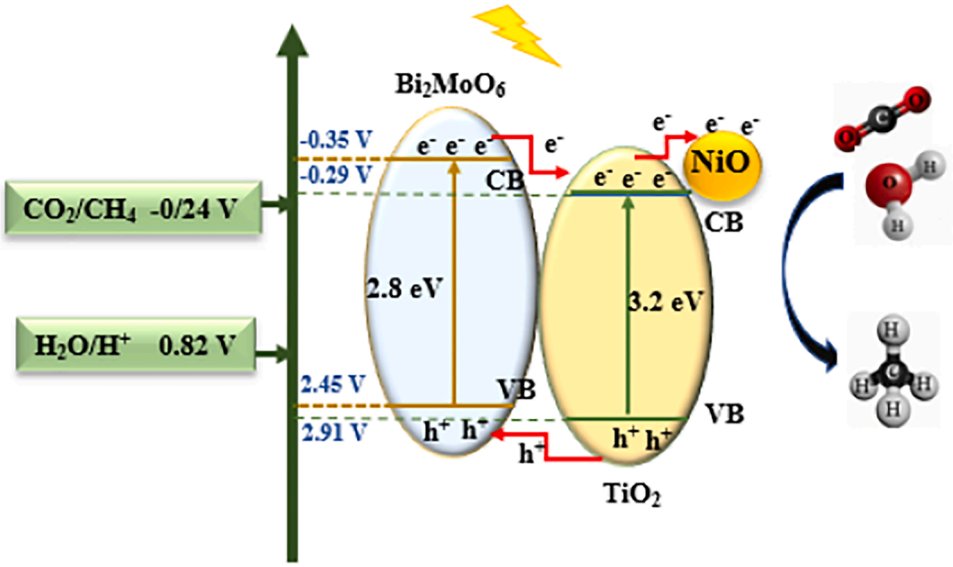

Fig. 13. Proposed charge transfer mechanism of CO_2 photoreduction over the Ni-BT catalyst. (Note: The mechanism is hypothetical and based on band structure calculations and literature reports; it has not been directly verified experimentally.).

the photogenerated charge carriers are highly transient and may rapidly recombine, limiting their contribution to redox reactions. Alternatively, these carriers can be immobilized at the surface of metallic species, where they actively participate in oxidation-reduction pathways. It should be emphasized that this mechanism is hypothetical, based on band structure calculations and literature reports, and has not been directly verified experimentally. The catalyst plays a pivotal role by capturing electrons, thereby prolonging their lifetime and ensuring a greater fraction of them engage in the CO_2 reduction process [54].

3.3. Ultrasound modification effect

Fig. 14 illustrates the impact of ultrasonic treatment on the structural characteristics of the photocatalyst. A comparative assessment of the XRD patterns of Ni-BT and Ni-BT(I) revealed that sonication reduced the crystallinity of the sample, suggesting a more uniform distribution of Ni nanoparticles on the catalyst surface [75,104]. This finding was supported by FESEM and EDX analyses. The use of ultrasonic irradiation allowed for a more even dispersion of co-catalyst species and increased the availability of reactant molecules to photogenerated charge carriers, leading to a notable improvement in methane yield.

Fig. 15 presents the morphology of the Ni-BT(I) sample prepared via

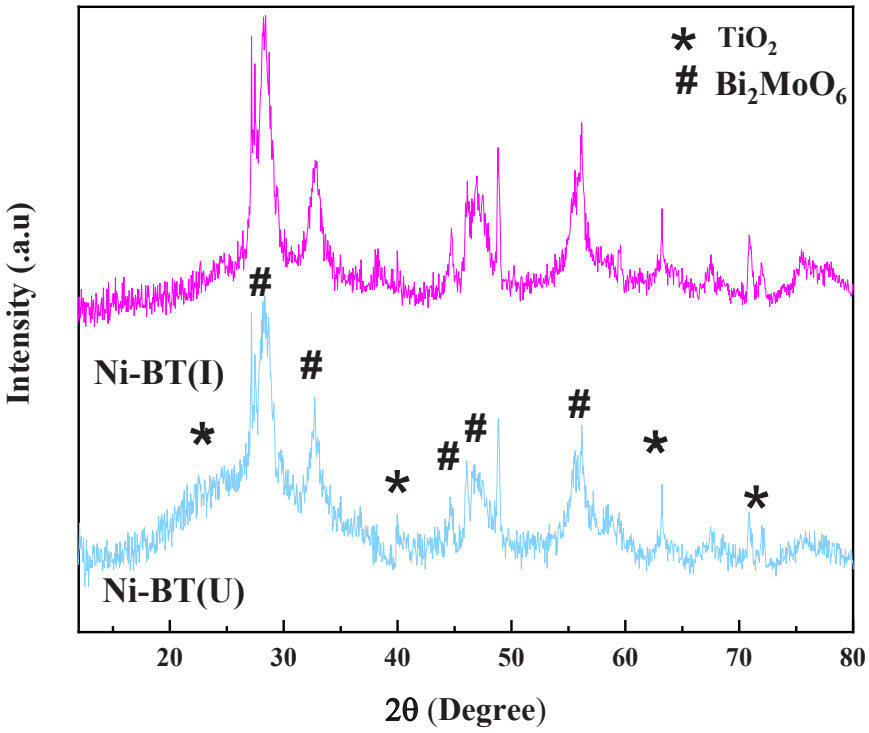

Fig. 14. XRD patterns of Ni-BT(I) and Ni-BT samples.

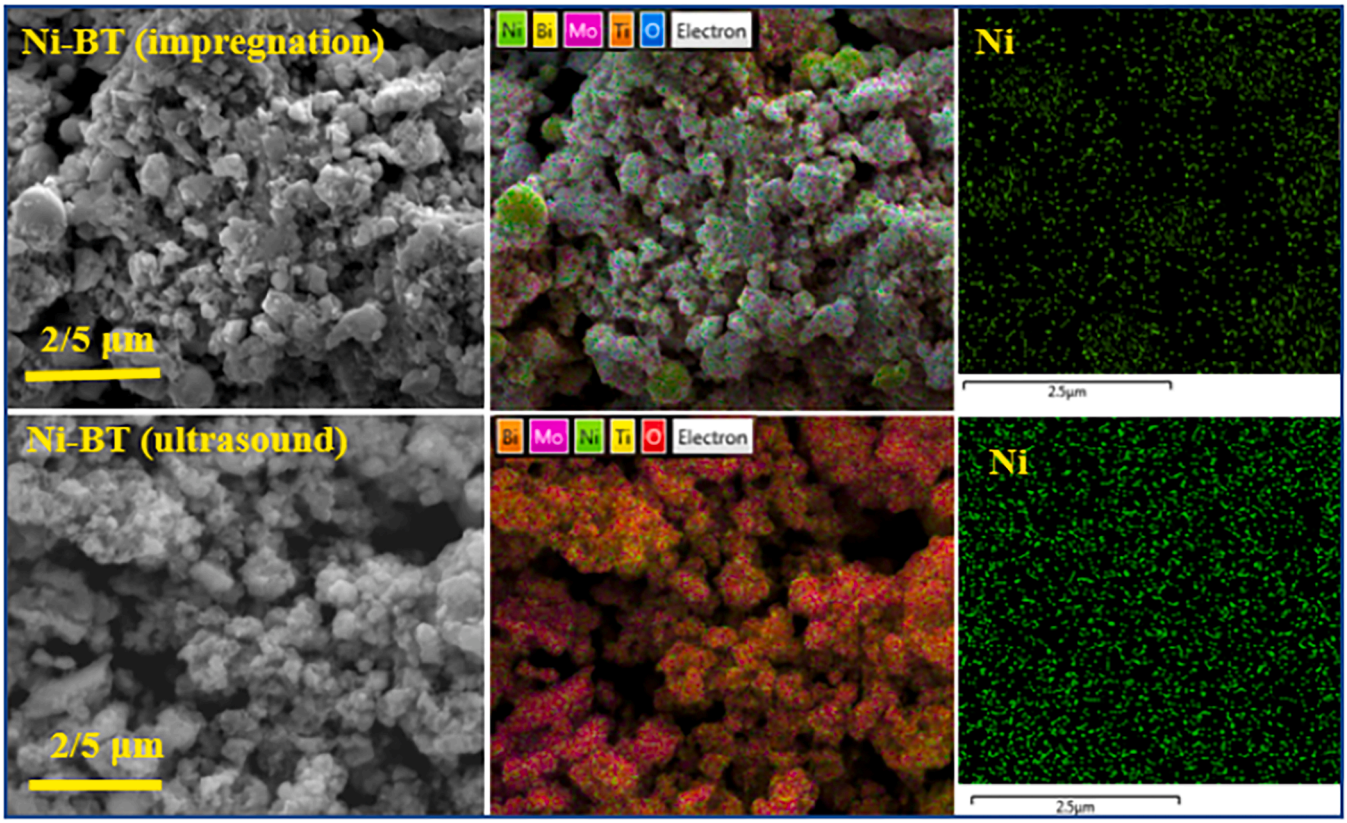

Fig. 15. FESEM and EDX analysis of Ni-BT(I) and Ni-BT samples.

the conventional impregnation method. The image reveals a relatively dense structure with evident surface agglomeration, which can be attributed to the clustering of co-catalyst particles during impregnation, resulting in larger and irregularly shaped particles. In contrast, the sample synthesized using ultrasonic irradiation (Ni-BT(U)) exhibits a more uniform and distinct morphology. The ultrasound treatment promotes the formation of smaller Ni particles and ensures their even distribution on the support, thereby reducing co-catalyst agglomeration and enhancing the accessibility of active sites on the photocatalytic surface.

Fig. 16 compares the photocatalytic activity of the Ni-BT samples prepared using ultrasound-assisted and conventional impregnation methods. The sample synthesized under ultrasonic irradiation demonstrated significantly higher methane production than its counterpart prepared by impregnation. These results indicate that ultrasound treatment enhances the catalyst performance by promoting uniform dispersion of Ni nanoparticles on the BT support, thereby improving the accessibility of active sites and facilitating more efficient charge transfer during CO_2 photoreduction.

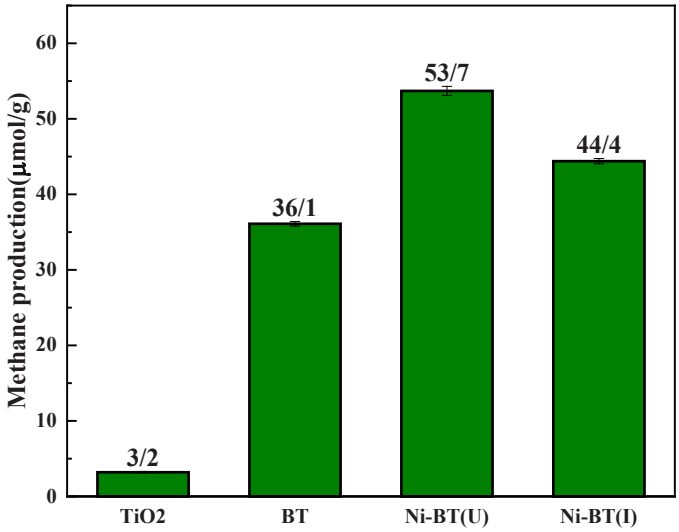

Fig. 16. CH_4 yield over different photo-catalysts after 8 h of reaction.

4. Conclusions

Ni, Ce, Co, Mo and Cu co-catalysts were successfully deposited on Bi_2MoO_6/TiO_2 composites using an ultrasound-assisted wet impregnation method. Their performance in CO_2 photoreduction to methane under UV-Vis light was then evaluated. The results showed that incorporating Bi_2MoO_6 onto TiO_2 enhanced the photocatalytic activity, attributed to the formation of a heterojunction between Bi_2MoO_6 and TiO_2. The ultrasound-assisted deposition of co-catalysts on the BT support led to a uniform distribution of nanoparticles, as confirmed by FESEM. EDX analysis also verified the homogeneous dispersion of co-catalyst species. The triple composites exhibited higher photocatalytic activity than the bare BT support, mainly due to improved light absorption and efficient charge separation. Different co-catalysts resulted in distinct structural and optical properties, leading to variations in photocatalytic performance. Among samples tested, Ni-BT showed the highest methane production of 53.7 μmol/g. This superior performance is primarily attributed to its narrower band gap and enhanced separation efficiency of photogenerated electron-hole pairs, which facilitated more effective CO_2 reduction.

CRediT authorship contribution statement

Seyed Mahdi Alavi: Supervision, Resources. **Maryam Ahmadi:** Writing – original draft, Investigation. **Azadeh Haghighatzadeh:** Writing – review & editing. **Ali Akbar Asgharinezhad:** Supervision. **Afsanehsadat Larimi:** Writing – review & editing, Supervision, Funding acquisition.

Declaration of Competing Interest

The authors declare that they have no known competing financial interests or personal relationships that could have appeared to influence the work reported in this paper.

Data Availability

Data will be made available on request.

References

[1] L. Li, F. Ye, Q. Lv, J. Xia, N. Chen, H. Wang, L. Chen, K. Zhao, Z. Zeng, M. Ahmad, Z. Xiao, S. Wang, Q. Zhang, Polydopamine-coated hollow carbon nitride as a full-spectral response photocatalyst for efficient H2O2 production via redox dual pathways, Appl. Catal. B Environ. Energy 363 (2025) 124802.

[2] L. Li, H. Zhang, F. Ye, Z. Xiao, Z. Zeng, H. Li, M. Ahmad, S. Wang, Q. Zhang, Few-layer meets crystalline structure: collaborative efforts for improving photocatalytic H2O2 generation over carbon nitride, ACS Appl. Mater. Interfaces 16 (2024) 17506–17516, https://doi.org/10.1021/acsami.3c19464.

[3] M. Ahmad, S. Chen, F. Ye, X. Quan, S. Afzal, H. Yu, X. Zhao, Efficient photo-Fenton activity in mesoporous MIL-100(Fe) decorated with ZnO nanosphere for pollutants degradation, Appl. Catal. B Environ. 245 (2019) 428–438.

[4] N. Chen, J. Xia, L. Li, Q. Lv, K. Zhao, M. Ahmad, Z. Xiao, S. Wang, F. Ye, Q. Zhang, Comprehensive enhancement of photocatalytic H_2O_2 generation and antibacterial efficacy on carbon nitride through a straightforward polydopamine coating strategy, Surf. Interfaces 56 (2025) 105566.

[5] F. Ye, Y. Liu, Q. Lv, B. Gao, J. Xia, X. Li, M. Dou, K. Zhao, M. Ahmad, Z. Xiao, S. Wang, S. Wang, Q. Zhang, Unveiling the mechanism of efficient detoxification by Pd species in chlorinated pollutant degradation, Chin. Chem. Lett. 37 (2026) 111136.

[6] Z. Zeng, L. Tan, F. Ye, M. Ahmad, X. Wang, D. Fang, H. Peng, S. Deng, H. Xiao, Carbon nitride with water soluble ability: enhanced oxygen species interphase mass transfer for homogenous photocatalytic water purification, Appl. Surf. Sci. 652 (2024) 159352.

[7] Z. Zeng, X. Xu, M. Huang, J. Mao, F. Ye, M. Ahmad, X. Wang, H. Peng, X. Lu, S. Deng, S. Dong, H. Xiao, Reversible sol–gel transitions mediated organics selective uptake and release for simultaneous water purification and chemicals recovery, Nano Lett. 25 (2025) 1451–1458, https://doi.org/10.1021/acs.nanolett.4c05347.

[8] M. Tasbihi, M. Schwarze, M. Edelmannová, C. Spöri, P. Strasser, R. Schomäcker, Photocatalytic reduction of CO2 to hydrocarbons by using photodeposited Pt nanoparticles on carbon-doped titania, Catal. Today (2019) 8–14, https://doi.org/10.1016/j.cattod.2018.10.011.

[9] A. Larimi, F. Khorasheh, Carbonaceous supports decorated with Pt–TiO2 nanoparticles using electrostatic self-assembly method as a highly visible-light active photocatalyst for CO2 photoreduction, Renew. Energy 145 (2020) 1862–1869, https://doi.org/10.1016/j.renene.2019.07.105.

[10] M. Tasbihi, K. Kočí, M. Edelmannová, I. Troppová, M. Reli, R. Schomäcker, Pt/TiO2 photocatalysts deposited on commercial support for photocatalytic reduction of CO2, J. Photochem. Photobiol. A Chem. 366 (2018) 72–80, https://doi.org/10.1016/j.jphotochem.2018.04.012.

[11] R. Nematollahi, C. Ghotbi, F. Khorasheh, A. Larimi, Ni-Bi co-doped TiO2 as highly visible light response nano-photocatalyst for CO2 photo-reduction in a batch photo-reactor, J. CO2 Util. 41 (2020) 101289, https://doi.org/10.1016/j.jcou.2020.101289.

[12] K. Li, B. Peng, T. Peng, Recent advances in heterogeneous photocatalytic CO2 conversion to solar fuels, ACS Catal. 6 (2016) 7485–7527, https://doi.org/10.1021/acscatal.6b02089.

[13] L. Zhang, Q. Shen, L. Yu, F. Huang, C. Zhang, J. Sheng, F. Zhang, D. Cheng, H. Yang, Fabrication of a high-adsorption N-TiO2/Bi2MoO6 composite photocatalyst with a hierarchical heterostructure for boosted weak-visible-light photocatalytic degradation of tetracycline, CrystEngComm 22 (2020) 5481–5490, https://doi.org/10.1039/d0ce00761g.

[14] M. Tahir, B. Tahir, N.A.S. Amin, A. Muhammad, Photocatalytic CO2 methanation over NiO/In2O3 promoted TiO2 nanocatalysts using H2O and/or H2 reductants, Energy Convers. Manag. 119 (2016) 368–378, https://doi.org/10.1016/j.enconman.2016.04.057.

[15] W.T. Chen, Y. Dong, P. Yadav, R.D. Aughterson, D. Sun-Waterhouse, G.I. N. Waterhouse, Effect of alcohol sacrificial agent on the performance of Cu/TiO2 photocatalysts for UV-driven hydrogen production, Appl. Catal. A Gen. 602 (2020) 117703, https://doi.org/10.1016/j.apcata.2020.117703.

[16] K. Kočí, H. Dang Van, M. Edelmannová, M. Reli, J.C.S. Wu, Photocatalytic reduction of CO2 using Pt/C3N4 photocatalyts, Appl. Surf. Sci. 503 (2020) 144426, https://doi.org/10.1016/j.apsusc.2019.144426.

[17] R. Vershney, K. Chelaramani, A. Bhardwaj, Synthesis, photocatalytic and antibacterial activities of nickel doped TiO2 nanoparticles, Orient J. Chem. 34 (6) (2018) 2.

[18] N.H. Aprilita, D. Amalia, E.T. Wahyuni, Removal of the hazardous Congo Red Dye through degradation under visible light photocatalyzed by C , N Co-doped TiO2 prepared from Chicken Egg White, Sci. World J. (2022) 14–17.

[19] S. Du, J. Lian, F. Zhang, Visible light-responsive N-doped TiO2 photocatalysis: synthesis, characterizations, and applications, Trans. Tianjin Univ. 28 (2022) 33–52, https://doi.org/10.1007/s12209-021-00303-w.

[20] M. Nurdin, L. Ode, A. Nur, D. Darmawati, Synthesis of Ni, N co-doped TiO2 using microwave-assisted method for sodium lauryl sulfate degradation by photocatalyst, J. Coat. Technol. Res. (2017), https://doi.org/10.1007/s11998-017-9976-8.

[21] T.P. Nguyen, D.L.T. Nguyen, V.H. Nguyen, T.H. Le, D.V.N. Vo, Q.T. Trinh, S. R. Bae, S.Y. Chae, S.Y. Kim, Q.Van Le, Recent advances in TiO2-based photocatalysts for reduction of CO2 to fuels, Nanomaterials 10 (2020) 1–24, https://doi.org/10.3390/nano10020337.

[22] O. Shtyka, R. Ciesielski, A. Kedziora, W. Maniukiewicz, S. Dubkov, D. Gromov, T. Maniecki, Photocatalytic reduction of CO2 over Me (Pt, Pd, Ni, Cu)/TiO2 catalysts, Top. Catal. 63 (2020) 113–120, https://doi.org/10.1007/s11244-020-01241-y.

[23] X. Chen, F. Jin, Photocatalytic reduction of carbon dioxide by titanium oxide-based semiconductors to produce fuels, Front. Energy 13 (2019) 207–220, https://doi.org/10.1007/s11708-019-0628-9.

[24] M. Ahmadi, S.Mehdi Alavi, A. Larimi, Pt–Cu@Bi2MoO6/TiO2 photocatalyst for CO2 reduction, Inorg. Chem. 62 (2023) 20372–20389, https://doi.org/10.1021/acs.inorgchem.3c03372.

[25] M. Ahmadi, S.M. Alavi, A. Larimi, Effective CO2 photoreduction to methane over Bi2MoO6/ Ni, N co-doped TiO2 nano-photocatalyst, Int. J. Hydrog. Energy 56 (2024) 1309–1323, https://doi.org/10.1016/j.ijhydene.2023.12.291.

[26] S. Salehian, A. Larimi, A.A. Asgharinezhad, N. Khallaghi, T.N. Borhani, C. Ghotbi, Magnetic Z-scheme bismuth molybdate(1-x)/Fe3O4@MIL-125(Ti)(x) nanocomposite as a high-performance visible-light-active photocatalyst for ultra-deep oxidative desulfurization of liquid fuel, Surf. Interfaces 42 (2023) 103432, https://doi.org/10.1016/j.surfin.2023.103432.

[27] M. Ahmadi, S. Mehdi, A. Larimi, UV–vis light responsive Bi2WO6 nanosheet/TiO2 nanobelt heterojunction photo-catalyst for CO2 reduction, Catal. Commun. 179 (2023) 106681, https://doi.org/10.1016/j.catcom.2023.106681.

[28] M. Ahmadi, S.M. Alavi, A. Larimi, Highly active platinum decorated BiVO4 nanosheet/TiO2 nanobelt heterojunction for photocatalytic CO2 reduction, Surf. Interfaces 45 (2024) 103908, https://doi.org/10.1016/j.surfin.2024.103908.

[29] M. Osanloo, F. Khorasheh, A. Larimi, Development of a novel Z-scheme TiO2/CuBi2O4@GO with enhanced performance for the photocatalytic degradation of metronidazole, J. Water Process Eng. 72 (2025) 107641, https://doi.org/10.1016/j.jwpe.2025.107641.

[30] M. Moradi, A. Larimi, F. Khorasheh, R. Nematollahi, Photocatalytic reduction of carbon dioxide to renewable methane using titanium dioxide modified with bismuth and copper, J. Appl. Res. Chem. Polym. Eng. 4 (2020). https://arcpe.modares.ac.ir/article-38-41281-en.html, 55-43 (accessed September 20, 2022).

[31] Y. Peng, Y. Zhang, F. Tian, J. Zhang, J. YuStructure Tuning of Bi2MoO6 and Their Enhanced Visible Light Photocatalytic Performances 84362017, 10.1080/10408436.2016.1200009.

[32] L. Ye, Y. Deng, L. Wang, H. Xie, F. Su, Bismuth-based photocatalysts for solar photocatalytic carbon dioxide conversion, ChemSusChem 12 (2019) 3671–3701, https://doi.org/10.1002/cssc.201901196.

[33] H. Li, T. Zhang, C. Pan, C. Pu, Y. Hu, X. Hu, E. Liu, J. Fan, Self-assembled Bi2MoO6/TiO2 nanofiber heterojunction film with enhanced photocatalytic activities, Appl. Surf. Sci. 391 (2017) 303–310, https://doi.org/10.1016/j.apsusc.2016.06.167.
[34] Y. Ao, J. Xu, P. Wang, C. Wang, J. Hou, J. Qian, Y. Li, Bi2MoO6 nanosheets deposited TiO2 nanobelts with spatially branched hierarchical heterostructure for enhanced photocatalytic activity under visible light irradiation, Colloids Surf. A Physicochem. Eng. Asp. 487 (2015) 66–74, https://doi.org/10.1016/j.colsurfa.2015.09.034.
[35] G. Fang, J. Liu, J. Wu, M. Li, X. Yan, D. Wang, A generic strategy for preparation of TiO 2 /Bi x M y O z (M = W, Mo) heterojunctions with enhanced photocatalytic activities, Appl. Surf. Sci. 475 (2019) 785–792, https://doi.org/10.1016/j.apsusc.2018.12.297.
[36] M. Abdollahi, A. Larimi, Z. Jiang, F. Khorasheh, C. Ghotbi, Photocatalytic oxidative desulfurization of model fuel over visible light-active Cu-impregnated carbon-doped TiO2, J. Clean. Prod. 380 (2022) 134968, https://doi.org/10.1016/j.jclepro.2022.134968.
[37] A. Ostovar, A. Larimi, Z. Jiang, M. Lotfi, C. Ghotbi, F. Khorasheh, Enhanced visible-light photocatalytic oxidative desulfurization of model fuel over Pt-decorated carbon-doped TiO2 nanoparticles, Environ. Sci. Pollut. Res. (2023), https://doi.org/10.1007/s11356-023-26597-y.
[38] A. Larimi, Chapter 6 - titanium-based nanophotocatalysts for CO2 conversion, in: S.A. Mazari, N.M. Mubarak, M.B.T.N. for C.D.C., C.T. Tripathi (Eds.), Micro Nano Technol, Elsevier, 2023, pp. 153–180, https://doi.org/10.1016/B978-0-323-89851-5.00008-1.
[39] S.M.M. Ahmadi, A. Larimi, A.A. Asgharinezhad, F. Khorasheh, C. Ghotbi, Inside- and outside-coated PANI and/or PIN-TiO2 nanotubes for enhanced photocatalytic degradation of 4-nitrophenol in wastewater, ACS Omega 9 (2024) 51320–51336, https://doi.org/10.1021/acsomega.4c08137.
[40] M. Osanloo, F. Khorasheh, A. Larimi, Fabrication of nano-dandelion magnetic TiO2/CuFe2O4 doped with silver as a highly visible-light-responsive photocatalyst for degradation of Naproxen and Rhodamine B, J. Mol. Liq. 407 (2024) 125242, https://doi.org/10.1016/j.molliq.2024.125242.
[41] L.J. Guo, Y.J. Wang, T. He, Photocatalytic reduction of CO2 over heterostructure semiconductors into value-added chemicals, Chem. Rec. (2016) 1918–1933, https://doi.org/10.1002/tcr.201600008.
[42] G. Yin, M. Nishikawa, Y. Nosaka, N. Srinivasan, D. Atarashi, E. Sakai, M. Miyauchi, Photocatalytic carbon dioxide reduction by copper oxide nanocluster-grafted niobate nanosheets, ACS Nano 9 (2015) 2111–2119, https://doi.org/10.1021/nn507429e.
[43] (an) S. He, P. Cao, J. Zhou, Yu, Recent advances in visible light Bi-based photocatalysts, Chin. J. Catal. 35 (2014) 989–1007, https://doi.org/10.1016/S1872-2067(14)60075-9.
[44] M. Hosseini, M. Haghighi, D. Kahforoushan, M. Zarrabi, Sono-dispersion of ceria and palladium in preparation and characterization of Pd/Al2O3-clinoptilolite-CeO2 nanocatalyst for treatment of polluted air via low temperature VOC oxidation, Process Saf. Environ. Prot. 106 (2017) 284–293, https://doi.org/10.1016/J.PSEP.2016.06.028.
[45] R. Akbari Sene, G.R. Moradi, S. Sharifnia, Sono-dispersion of TiO2 nanoparticles over clinoptilolite used in photocatalytic hydrogen production: effect of ultrasound irradiation during conventional synthesis methods, Ultrason. Sonochem. 37 (2017) 490–501, https://doi.org/10.1016/J.ULTSONCH.2017.02.006.
[46] S.V. Sancheti, C. Saini, R. Ambati, P.R. Gogate, Synthesis of ultrasound assisted nanostuctured photocatalyst (NiO supported over CeO2) and its application for photocatalytic as well as sonocatalytic dye degradation, Catal. Today (2017), https://doi.org/10.1016/j.cattod.2017.02.047.
[47] M. Alves Melo Júnior, A. Morais, A.F. Nogueira, Boosting the solar-light-driven methanol production through CO2 photoreduction by loading Cu2O on TiO2-pillared K2Ti4O9, Microporous Mesoporous Mater. 234 (2016) 1–11, https://doi.org/10.1016/J.MICROMESO.2016.06.043.
[48] E. Liu, L. Qi, J. Bian, Y. Chen, X. Hu, J. Fan, H. Liu, C. Zhu, Q. Wang, A facile strategy to fabricate plasmonic Cu modified TiO2 nano-flower films for photocatalytic reduction of CO2 to methanol, Mater. Res. Bull. 68 (2015) 203–209, https://doi.org/10.1016/j.materresbull.2015.03.064.
[49] I. Shown, H.-C. Hsu, Y.-C. Chang, C.-H. Lin, P.K. Roy, A. Ganguly, C.-H. Wang, J.-K. Chang, C.-I. Wu, L.-C. Chen, K.-H. Chen, Highly efficient visible light photocatalytic reduction of CO2 to hydrocarbon fuels by Cu-nanoparticle decorated graphene oxide, Nano Lett. 14 (2014) 6097–6103, https://doi.org/10.1021/nl503609v.
[50] D. Liu, Y. Fernández, O. Ola, S. Mackintosh, M. Maroto-Valer, C.M.A. Parlett, A. F. Lee, J.C.S. Wu, On the impact of Cu dispersion on CO2 photoreduction over Cu/TiO2, Catal. Commun. 25 (2012) 78–82, https://doi.org/10.1016/J.CATCOM.2012.03.025.
[51] H. Liu, X. Meng, T.D. Dao, L. Liu, P. Li, G. Zhao, T. Nagao, L. Yang, J. Ye, Light assisted CO2 reduction with methane over SiO2 encapsulated Ni nanocatalysts for boosted activity and stability, J. Mater. Chem. A Mater. Energy Sustain. 00 (2017) 1–7, https://doi.org/10.1039/C7TA00704C.
[52] J. Albero, H. Garcia, A. Corma, Temperature dependence of solar light assisted CO2 reduction on Ni based photocatalyst, Top. Catal. 59 (2016) 787–791, https://doi.org/10.1007/s11244-016-0550-x.
[53] D. Lee, H. Chen, Y. Chen, Journal of physics and chemistry of solids photocatalytic reduction of carbon dioxide with water using InNbO4 catalyst with NiO and Co3O4 cocatalysts, J. Phys. Chem. Solids 73 (2012) 661–669, https://doi.org/10.1016/j.jpcs.2012.01.005.
[54] X. Shao, X. Yin, J. Wang, Nanoheterostructures of potassium tantalate and nickel oxide for photocatalytic reduction of carbon dioxide to methanol in isopropanol, J. Colloid Interface Sci. (2017), https://doi.org/10.1016/j.jcis.2017.10.057.
[55] N. Singhal, R. Goyal, U. Kumar, Visible-light-assisted photocatalytic CO2 reduction over InTaO4: selective methanol formation, Energy Fuels 31 (2017) 12434–12438, https://doi.org/10.1021/acs.energyfuels.7b02123.
[56] M. Beshtar, A.Akbar Asgharinezhad, A. Larimi, Ultra-deep photocatalytic oxidative desulfurization of liquid fuels by Ti@CeO2/ZnO nanophotocatalyst under visible light and mild operating conditions, J. Ind. Eng. Chem. (2024), https://doi.org/10.1016/j.jiec.2024.01.017.
[57] M. Beshtar, F. Khorasheh, A. Larimi, A. Akbar Asgharinezhad, Photocatalytic oxidative desulfurization of model fuel using iron-molybdenum nanocatalyst based on cerium oxide (FeyMox/CeO2) under visible light, Fuel 360 (2024) 130549, https://doi.org/10.1016/j.fuel.2023.130549.
[58] M. Beshtar, A. Larimi, A.A. Asgharinezhad, F. Khorasheh, Ultra-deep photocatalytic oxidative desulfurization of model fuel using Ti-UiO-66(Zr) metal–organic framework, Catal. Lett. (2023), https://doi.org/10.1007/s10562-023-04506-9.
[59] L.I. Ibarra-rodriguez, J.C. Pantoja-espinoza, E. Lu, L.M. Torres-martínez, L. F. Garay-rodríguez, L. Alejandro, V.H. Collins-martínez, Formic acid and hydrogen generation from the photocatalytic reduction of CO2 on visible light activated N-TiO2/CeO2/CuO composites, J. Photochem. Photobiol. 11 (2022) 100125, https://doi.org/10.1016/j.jpap.2022.100125.
[60] S. Ijaz, M.F. Ehsan, M.N. Ashiq, N. Karamat, T. He, Preparation of composite for photocatalytic reduction of CO2 under visible-light irradiation, Appl. Surf. Sci. (2016), https://doi.org/10.1016/j.apsusc.2016.08.098.
[61] Y. Wang, J. Zhao, T. Wang, Y. Li, X. Li, J. Yin, C. Wang, CO2 photoreduction with H2O vapor on highly dispersed CeO2/TiO2 catalysts: surface species and their reactivity, J. Catal. 337 (2016) 293–302, https://doi.org/10.1016/j.jcat.2015.12.030.
[62] H. Abdullah, M.R. Khan, M. Pudukudy, Z. Yaakob, N.A. Ismail, CeO2-TiO2 as a visible light active catalyst for the photoreduction of CO2 to methanol 33 (2015) 1155–1161, https://doi.org/10.1016/S1002-0721(14)60540-8.
[63] G. Yang, S. Wang, Y. Wu, H. Zhou, W. Zhao, S. Zhong, L. Liu, S. Bai, Spatially separated redox cocatalysts on ferroelectric nanoplates for improved piezophotocatalytic CO2 reduction and H2O oxidation, ACS Appl. Mater. Interfaces 15 (2023) 14228–14239, https://doi.org/10.1021/acsami.2c20685.
[64] A.F.S. Molouk, J. Yang, T. Okanishi, H. Muroyama, T. Matsui, K. Eguchi, Comparative study on ammonia oxidation over Ni-based cermet anodes for solid oxide fuel cells, J. Power Sources 305 (2016) 72–79, https://doi.org/10.1016/j.jpowsour.2015.11.085.
[65] H. Rastgaran, N. Fatoorehchi, A. Khallaghi, T.N. Larimi, Borhani, Modelling of photocatalytic CO2 reduction into value-added products in a packed bed photoreactor using the ray tracing method, Carbon Capt. Sci. Technol. A (2023) 100118, https://doi.org/10.1016/j.ccst.2023.100118.
[66] A. Asadi, A. Larimi, Z. Jiang, A. Naderifar, Modeling and simulation of photocatalytic CO2 reduction into methanol in a bubble slurry photoreactor, Chem. Eng. Sci. 263 (2022) 118078, https://doi.org/10.1016/J.CES.2022.118078.
[67] D. Zhao, X. Zhang, L. Sui, W. Wang, X. Zhou, X. Cheng, S. Gao, Y. Xu, L. Huo, carbon chains and their sensing mechanism analysis, Sens. Actuators B Chem. 312 (2020) 127942, https://doi.org/10.1016/j.snb.2020.127942.
[68] Z. Zhao, W. Zhang, X. Shen, T. Muhmood, M. Xia, W. Lei, F. Wang, M.A. Khan, Preparation of g-C3N4/TiO2/BiVO4 composite and its application in photocatalytic degradation of pollutant from TATB production under visible light irradiation, J. Photochem. Photobiol. A Chem. 358 (2018) 246–255, https://doi.org/10.1016/j.jphotochem.2018.03.028.
[69] Z. Yin, S. Qi, S. Deng, K. Xu, Z. Liu, M. Zhang, Z. Sun, Bi2MoO6/TiO2 heterojunction modified with Ag quantum dots: a novel photocatalyst for the efficient degradation of tetracycline hydrochloride, J. Alloy. Compd. 888 (2021) 161582, https://doi.org/10.1016/j.jallcom.2021.161582.
[70] Y. Li, T. Cao, Z. Mei, X. Li, D. Sun, Separating type I heterojunction of NaBi(MoO4)2/Bi2MoO6 by TiO2 nanofibers for enhanced visible-photocatalysis, Chem. Phys. 533 (2020), https://doi.org/10.1016/j.chemphys.2020.110696.
[71] S. Chen, J. Yu, J. Zhang, Enhanced photocatalytic CO2 reduction activity of MOF-derived ZnO/NiO porous hollow spheres, J. CO2 Util. 24 (2018) 548–554, https://doi.org/10.1016/j.jcou.2018.02.013.
[72] F. Rahmani, M. Haghighi, S. Mahboob, CO2-enhanced dehydrogenation of ethane over sonochemically synthesized Cr/clinoptilolite-ZrO2 nanocatalyst: Effects of ultrasound irradiation and ZrO2 loading on catalytic activity and stability, Ultrason. Sonochem. 33 (2016) 150–163, https://doi.org/10.1016/J.ULTSONCH.2016.04.034.
[73] M. Ahmadi, M. Haghighi, D. Kahforoushan, Influence of active phase composition (Mn, Ni, MnxNi10−x) on catalytic properties and performance of clinoptilolite supported nanocatalysts synthesized using ultrasound energy toward abatement of toluene from polluted air, Process Saf. Environ. Prot. 106 (2017) 294–308, https://doi.org/10.1016/J.PSEP.2016.06.029.
[74] A.I. Journal, L. Wang, M.N. Ha, Z. Liu, Z. Zhao, Mesoporous WO3 modified by Mo for enhancing reduction of CO2 to solar fuels under visible light and thermal conditions, Integr. Ferroelectr. Int. J. 4587 (2016), https://doi.org/10.1080/10584587.2016.1176507.
[75] L. Yosefi, M. Haghighi, S. Allahyari, S. Ashkriz, Effect of ultrasound irradiation and Ni-loading on properties and performance of CeO2-doped Ni/clinoptilolite nanocatalyst used in polluted air treatment, Process Saf. Environ. Prot. 95 (2015) 26–37, https://doi.org/10.1016/J.PSEP.2015.02.006.

[76] J. Tauc, R. Grigorovici, A. Vancu, Optical Properties and Electronic Structure of Amorphous Germanium, Phys. Status Solidi 15 (1966) 627–637, https://doi.org/10.1002/pssb.19660150224.
[77] R. López, R. Gómez, Band-gap energy estimation from diffuse reflectance measurements on sol–gel and commercial TiO2: a comparative study, J. Sol. Gel Sci. Technol. 61 (2012) 1–7, https://doi.org/10.1007/s10971-011-2582-9.
[78] Z. He, C. Jiang, K. Wang, Z. Wang, N. Li, W. Wang, Z. LiuPhotothermal CO2 hydrogenation to methanol over a CoO/Co/TiO2 catalyst in aqueous media under atmospheric pressure2020.
[79] S. Ali, J. Lee, H. Kim, Y. Hwang, A. Razzaq, J.W. Jung, C.H. Cho, S.Il In, Sustained, photocatalytic CO2 reduction to CH4 in a continuous flow reactor by earth-abundant materials: Reduced titania-Cu2O Z-scheme heterostructures, Appl. Catal. B Environ. 279 (2020), https://doi.org/10.1016/j.apcatb.2020.119344.
[80] A. Sharma, B.K. Lee, Photocatalytic reduction of carbon dioxide to methanol using nickel-loaded TiO2 supported on activated carbon fiber, Catal. Today 298 (2017) 158–167, https://doi.org/10.1016/j.cattod.2017.05.003.
[81] M. Tahir, N.S. Amin, Performance analysis of nanostructured NiO-In2O3/TiO2 catalyst for CO2 Photoreduction with H2 in a Monolith photoreactor, Chem. Eng. J. (2015), https://doi.org/10.1016/j.cej.2015.10.033.
[82] S. Milad, Q.A. Yousif, H. Abbas, A. Al-nayili, M. Salavati-niasari, Ultrasound-assisted fabrication and characterization of a novel UV-light-responsive Er2Cu2O5 semiconductor nanoparticle photocatalyst, Arab. J. Chem. 15 (2022) 103826, https://doi.org/10.1016/j.arabjc.2022.103826.
[83] H. Lin, C. Shih, Chemical Efficient one-pot microwave-assisted hydrothermal synthesis of M (M = Cr, Ni, Cu, Nb) and nitrogen co-doped TiO2 for hydrogen production by photocatalytic water splitting, J. Mol. Catal. A. Chem. 411 (2016) 128–137, https://doi.org/10.1016/j.molcata.2015.10.026.
[84] X. Li, Z. Zhuang, W. Li, H. Pan, Photocatalytic reduction of CO2 over noble metal-loaded and nitrogen-doped mesoporous TiO2, Appl. Catal. A Gen. 429-430 (2012) 31–38, https://doi.org/10.1016/j.apcata.2012.04.001, 3138.
[85] M. Fakhrul Ridhwan Samsudin, S. Sufian, R. Bashiri, N. Muti Mohamed, L. Tau Siang, R. Mahirah Ramli, Optimization of photodegradation of methylene blue over modified TiO2/BiVO4 photocatalysts: effects of total TiO2 loading and different type of co-catalyst, Mater. Today Proc. 5 (2018) 21710–21717, https://doi.org/10.1016/j.matpr.2018.07.023.
[86] J. Chen, Y. Zhang, Z. Zhang, D. Hou, F. Bai, Y. Han, C. Zhang, Y. Zhang, J. Hu, Metal–support interactions for heterogeneous catalysis: mechanisms, characterization techniques and applications, J. Mater. Chem. A. 11 (2023) 8540–8572, https://doi.org/10.1039/D2TA10036C.
[87] T. Wang, J. Hu, R. Ouyang, Y. Wang, Y. Huang, S. Hu, W.-X. Li, Nature of metal-support interaction for metal catalysts on oxide supports, Science 386 (80) (2024) 915–920, https://doi.org/10.1126/science.adp6034.
[88] L. Zhuo, S. Dong, Y.T. Sham, J. Zhang, X. Xu, K.C.K. Ho, M. Pan, Q. Chen, G. Huang, J. Bi, Internal electric field steering S-scheme charge transfer in ZnIn2S4/COF boosts H2O2 photosynthesis from water and air for sustainable disinfection, Npj Clean. Water 8 (2025) 5, https://doi.org/10.1038/s41545-025-00437-7.
[89] A. Liu, X. Ma, B. Shen, H. Du, X. Jiang, Y. Wu, Y. Jin, J. Li, H. Zhu, Q. Wang, Sustainable dual-cathode photoelectro-Fenton system enabling oxidative and reductive removal of pollutants via visible light driving Fe sites conversion, Chem. Eng. J. 504 (2025) 158929, https://doi.org/10.1016/j.cej.2024.158929.
[90] L. Jin, M. Deng, J. Gao, L. Wang, Q. Zhou, X. Tang, Q. Li, H. Du, D. Hao, Q. Wang, A crystalline triazine covalent organic framework with partial fluorination for efficient hydrogen peroxide production toward water treatment, Chem. Eng. J. 515 (2025) 163722, https://doi.org/10.1016/j.cej.2025.163722.
[91] Y. Li, H. Wang, J. Xie, J. Hou, X. Song, D.D. Dionysiou, Bi2WO6-TiO2/starch composite films with Ag nanoparticle irradiated by γ-ray used for the visible light photocatalytic degradation of ethylene, Chem. Eng. J. 421 (2021) 129986, https://doi.org/10.1016/j.cej.2021.129986.
[92] L. Cheng, L. Liu, D. Wang, F. Yang, J. Ye, Synthesis of bismuth molybdate photocatalysts for CO 2 photo-reduction, J. CO2 Util. 29 (2019) 196–204, https://doi.org/10.1016/j.jcou.2018.12.013.
[93] X. Yang, S. Wang, N. Yang, W. Zhou, P. Wang, K. Jiang, S. Li, H. Song, X. Ding, H. Chen, J. Ye, Oxygen vacancies induced special CO2 adsorption modes on Bi2MoO6 for highly selective conversion to CH4, Appl. Catal. B Environ. 259 (2019) 118088, https://doi.org/10.1016/j.apcatb.2019.118088.
[94] R. Fiorenza, M. Bellardita, S. Andrea, L. Spitaleri, A. Gulino, M. Condorelli, L. D. Urso, S. Scir, L. Palmisano, A solar photothermocatalytic approach for the CO2 conversion: investigation of different synergisms on CoO-CuO/brookite TiO2-CeO2 catalysts 428 (2022), https://doi.org/10.1016/j.cej.2021.131249.
[95] S. Wang, Y. Zhang, Y. Zheng, Y. Xu, G. Yang, S. Zhong, Y. Zhao, S. Bai, Plasmonic metal mediated charge transfer in stacked core–shell semiconductor heterojunction for significantly enhanced CO2 photoreduction, Small 19 (2023) 2204774, https://doi.org/10.1002/SMLL.202204774.
[96] Z.U. Rehman, M. Bilal, J. Hou, F.K. Butt, J. Ahmad, S. Ali, A. Hussain, Photocatalytic CO2 reduction Using TiO2-based photocatalysts and TiO2 Z-scheme heterojunction composites: a review, Molecules 27 (2022) 2069, https://doi.org/10.3390/molecules27072069.
[97] F. Platero, A. Caballero, G. Colón, Tuning the co-catalyst loading for the optimization of thermo-photocatalytic hydrogen production over Cu/TiO2, Appl. Catal. A Gen. 643 (2022) 118804, https://doi.org/10.1016/j.apcata.2022.118804.
[98] S. Zhu, W. Liao, M. Zhang, S. Liang, Design of spatially separated Au and CoO dual cocatalysts on hollow TiO2 for enhanced photocatalytic activity towards the reduction of CO2 to CH4, Chem. Eng. J. (2018), https://doi.org/10.1016/j.cej.2018.12.095.
[99] X. Zhang, G. Ren, C. Zhang, R. Li, Q. Zhao, C. Fan, Photocatalytic reduction of CO2 to CO over 3D Bi2MoO6 microspheres: simple synthesis, high efficiency and selectivity, reaction mechanism, Catal. Lett. 150 (2020) 2510–2516, https://doi.org/10.1007/s10562-020-03182-3.
[100] Y. Gao, K. Qian, B. Xu, Z. Li, J. Zheng, S. Zhao, F. Ding, Y. Sun, Z. Xu, Recent advances in visible-light-driven conversion of CO2 by photocatalysts into fuels or value-added chemicals, Carbon Resour. Convers. 3 (2020) 46–59, https://doi.org/10.1016/j.crcon.2020.02.003.
[101] B. Shen, H. Du, A. Liu, N. Li, C. Chen, L. Shen, Y. Hui, R. Huo, Z. Zhang, Q. Wang, Interfacial electric field steering S-scheme charge transfer in MIL-88A(Fe)/polydopamine heterojunctions: dual-redox pathways for efficient pollutant mineralization, J. Clean. Prod. 523 (2025) 146458, https://doi.org/10.1016/j.jclepro.2025.146458.
[102] H. Du, Y. Hui, B. Shen, C. Chen, L. Shen, A. Liu, D. Hao, R. Huo, Z. Zhang, Q. Wang, Self-sustaining photo-Fenton system with built-in electric field optimized charge separation for continuous-flow water purification, Appl. Catal. B Environ. Energy 380 (2026) 125793, https://doi.org/10.1016/j.apcatb.2025.125793.
[103] H. Du, B. Shen, R. Huo, Y. Hui, C. Chen, A. Liu, Z. Zhang, C. Li, B. Ni, D. Hao, Q. Wang, Strong hetero-interfacial interactions mediated photocatalytic 3-electron oxygen reduction to hydroxyl radicals for wastewater decontamination, Appl. Catal. B Environ. Energy 379 (2025) 125688, https://doi.org/10.1016/j.apcatb.2025.125688.
[104] F. Rahmani, M. Haghighi, C2H6/CO2 oxidative dehydrogenation (ODH) reaction on nanostructured CrAPSO-34 catalyst: one-pot hydrothermal vs. conventional hydrothermal/impregnation catalyst synthesis, Korean J. Chem. Eng. 33 (2016) 2555–2566, https://doi.org/10.1007/s11814-016-0125-3.